August 11, 2006 Version 3.2

An Ultraviolet-to-Radio Broadband Spectral Atlas of Nearby Galaxies

D.A. Dale[1], A. Gil de Paz[2], K.D. Gordon[3], H.M. Hanson[1], L. Armus[4], G.J. Bendo[5], L. Bianchi[6], M. Block[3], S. Boissier[7], D. Calzetti[8], C.W. Engelbracht[3], G. Helou[9], T.H. Jarrett[4], R.C. Kennicutt[10,3], C. Leitherer[8], B.F. Madore[7], D.C. Martin[11], M.J. Meyer[8], E.J. Murphy[12], M.W. Regan[8], J.D.T. Smith[3], M.L. Sosey[8], D.A. Thilker[6] et al.

ABSTRACT

The ultraviolet-to-radio continuum spectral energy distributions are presented for all 75 galaxies in the *Spitzer* Infrared Nearby Galaxies Survey (SINGS). A principal component analysis of the sample shows that most of the sample's spectral variations stem from two underlying components, one representative of a galaxy with a low infrared-to-ultraviolet ratio and one representative of a galaxy with a high infrared-to-ultraviolet ratio. The influence of several parameters on the infrared-to-ultraviolet ratio is studied (e.g., optical morphology, disk inclination, far-infrared color, ultraviolet spectral slope, and star formation history). Similar to previous findings on normal star-forming galaxies, compared to starbursting galaxies the SINGS sample shows a larger dispersion in a plot of infrared-to-ultraviolet versus ultraviolet spectral slope. Much of this dispersion derives from the quiescent, early-type galaxies in the SINGS sample, which show significantly redder ultraviolet spectral slopes than do starbursts at a given infrared-to-ultraviolet ratio. Early-type galaxies also show the highest optical-to-infrared ratios and the smallest specific star formation rates. These results suggest that the star formation

[1]Department of Physics and Astronomy, University of Wyoming, Laramie, WY 82071; ddale@uwyo.edu

[2]Departamento de Astrofisica, Universidad Complutense, Avenida de la Complutense s/n, Madrid, E-28040, Spain

[3]Steward Observatory, University of Arizona, 933 North Cherry Avenue, Tucson, AZ 85721

[4]Spitzer Science Center, California Institute of Technology, M.S. 220-6, Pasadena, CA 91125

[5]Astrophysics Group, Imperial College, Blackett Laboratory, Prince Consort Road, London SW7 2AZ United Kingdom

[6]Center for Astrophysical Sciences, The Johns Hopkins University, 3400 N. Charles St., Baltimore, MD 21218

[7]Carnegie Observatories, Carnegie Institution of Washington, 813 Santa Barbara Street, Pasadena, CA 91101

[8]Space Telescope Science Institute, 3700 San Martin Drive, Baltimore, MD 21218

[9]California Institute of Technology, MC 314-6, Pasadena, CA 91101

[10]Institute of Astronomy, University of Cambridge, Cambridge CB3 0HA, United Kingdom

[11]Astronomy Option, California Institute of Technology, MS 105-24, Pasadena, CA 91125

[12]Department of Astronomy, Yale University, New Haven, CT 06520

history may be the dominant regulator of the broadband spectral variations between galaxies. Finally, a new discovery shows that the 24 μm morphology (smooth, clumpy, or unresolved) can be a useful tool for parametrizing the global dust temperature and ultraviolet extinction in nearby galaxies. The dust emission in dwarf/irregular galaxies is clumpy and warm, while in spiral galaxies there is typically a much larger diffuse component of cooler dust. For early-type galaxies with a single nuclear clump of 24 μm emission the dust temperature and ultraviolet extinction are quite high.

Subject headings: infrared: galaxies — infrared: ISM — ultraviolet: galaxies — galaxies: photometry

1. Introduction

Dust has always presented challenges to astronomy. Extinction makes it difficult to extract intrinsic fluxes. Reddening leads to uncertain colors. An outstanding challenge is to identify dust emission features (diffuse interstellar bands) that were discovered over 80 years ago. Nonetheless, interstellar dust also provides unique opportunities for understanding galaxy structure and evolution. The formation of molecules, interstellar heating and cooling processes, polarization, and photometric redshift indicators are just a few of the areas of study that benefit from the presence and knowledge of interstellar grains (see Draine 2003 for a review).

Though dust primarily releases energy over infrared and submillimeter wavelengths, much of the radiation intercepted by interstellar grains originates in the ultraviolet from the atmospheres of OB stars. Thus the combination of infrared and ultraviolet data presents interesting challenges and opportunities. One important application is determining ultraviolet-based star formation rates corrected for dust extinction. High redshift surveys carried out in the rest-frame ultraviolet and optical, for example, are particularly vulnerable to the presence of interstellar dust (e.g., Adelberger & Steidel 2000). Fortunately, studies coupling infrared and ultraviolet data have shown that the slope of the ultraviolet continuum is one such useful probe of the extinction in starburst galaxies (e.g., Calzetti, Kinney, & Storchi-Bergmann 1994; Meurer, Heckman, & Calzetti 1999; Gordon et al. 2000). Subsequent work in this area has explored how the infrared-to-ultraviolet ratio and its scatter depend on bolometric and monochromatic luminosity, ultraviolet spectral slope, metallicity, diameter, star formation rate, etc. (e.g., Buat et al. 2002; Bell 2003; Gordon et al. 2004; Kong et al. 2004; Buat et al. 2005; Calzetti et al. 2005; Seibert et al. 2005; Cortese et al. 2006; Schmitt et al. 2006; Iglesias-Páramo et al. 2006). One consistent result relevant to the work presented below is that normal star-forming (non-starburst) galaxies show larger scatter in plots of the infrared-to-ultraviolet ratio as a function of the ultraviolet spectral slope, with normal galaxies systematically exhibiting redder slopes. This broadening in the trend has been attributed to geometry, integrated versus local extractions, and/or the increased fractional contributions from recent (versus current) star formation, and (e.g., Bell et al. 2002; Kong et al. 2004; Calzetti et al. 2005; Seibert et al.

2005; Boissier et al. 2006).

We are interested in exploring how the infrared-to-ultraviolet ratio depends on quantities like morphology, color, and geometry within the SINGS sample (Kennicutt et al. 2003). But in broader terms, the main focus of this paper is to simply present a panchromatic atlas of the broadband spectral energy distributions of a large, diverse sample of nearby galaxies, and to quantify the variety of spectral shapes evident in such a sample. Since the fluxes presented in this work span wavelengths from the far-ultraviolet to the radio and are integrated over entire galaxies, this dataset should prove useful to astronomers studying galaxies at high redshifts, where only information on the global properties of galaxies is accessible and the rest-frame ultraviolet data are shifted into optical bandpasses. One may plausibly argue that the variety of luminosities and spectral shapes typically seen in high redshift surveys will be narrower than the diversity presented below for the SINGS sample, since flux-limited surveys at high redshifts will mainly be sampling luminous and infrared-warm systems. On the other hand, deep far-infrared surveys show significant numbers of higher redshift systems similar to local normal star-forming galaxies in mass, size, and dust temperature (e.g., Chapman et al. 2002; Sajina et al. 2006). In either case, the rich collection of *Spitzer*, GALEX, and ancillary data provided by the SINGS project represents an important panchromatic baseline for extragalactic work.

Section 2 presents the SINGS sample while Section 3 presents the collection of ultraviolet, optical, near-infrared, infrared, submillimeter, and radio data. The analysis of the broadband spectral energy distributions is described in Section 4 and the infrared-to-ultraviolet ratio is explored in detail in Section 5. A discussion and summary of the main results are provided in Section 6.

2. The Sample

The 75 galaxies in the *Spitzer* Nearby Galaxies Survey (SINGS; Kennicutt et al. 2003) come from a wide range of environments and galaxy types: low-metallicity dwarfs; quiescent ellipticals; dusty grand design spirals; Seyferts, LINERs, and star-forming nuclei of normal galaxies; and systems within the Local and M 81 groups (Table 1). The selection of the collection of 75 SINGS galaxies aimed to span a wide range in three key parameters (optical morphology, luminosity, infrared-to-optical color) and to adequately sample several other secondary parameters (e.g., infrared color, metallicity, surface brightness, inclination, bar structure, etc.). The SINGS sample is comprised of nearby galaxies, with a median distance of $\sim$10 Mpc and a maximum distance of only 30 Mpc.

3. The Data

Tables 2-3 present the global flux densities for the entire SINGS sample, for wavelengths spanning the ultraviolet through the radio. The data are corrected for Galactic extinction (Schlegel,

Finkbeiner, & Davis 1998) assuming $A_V/E(B-V) \approx 3.1$ and the reddening curve of Li & Draine (2001). The effect of airmass has been removed from the (optical and near-infrared) ground-based fluxes. Below follows a description of the new ultraviolet and optical and archival radio data collected for the SINGS program, in addition to a few updates to the *Spitzer* data presented in Dale et al. (2005).

3.1. Ultraviolet Data

The GALEX mission (Martin et al. 2005) is performing an all-sky survey at ultraviolet wavelengths. The imaging portion of the survey is being carried out with a far-ultraviolet and a near-ultraviolet filter respectively centered at 1528 and 2271 Å. In addition to imaging the entire sky with an effective exposure time of ∼0.1 ksec, GALEX is also carrying out relatively deep integrations (∼1.5 ksec) for a few hundred nearby galaxies, including nearly the entire SINGS sample. With an angular resolution of 4-6″, the spatial details in GALEX images are well matched to those seen in *Spitzer* 24 μm imaging and more resolved than in *Spitzer* 70 and 160 μm images. At the median distance of the SINGS sample (∼10 Mpc), the GALEX and MIPS 24 μm data probe spatial scales of about ∼300 pc. This resolution coupled with the GALEX field-of-view of 1.°25 allow for robust measures of sky-subtracted, integrated ultraviolet fluxes even for large nearby galaxies.

Integrated ultraviolet fluxes are computed from the surface photometry profiles derived for the *GALEX Atlas of Nearby Galaxies* (Gil de Paz et al. 2006).[1] Table 2 lists the global fluxes that include an asymptotic extrapolation to the isophotal profiles. The extrapolations are typically small and result in asymptotic fluxes that are, on average, 14% larger than those obtained at the optical radius; $\langle f_{\rm UV}({\rm asymptotic})/f_{\rm UV}(R_{25})\rangle = 1.14$ with a dispersion of 0.16 and 0.14 in the far- and near-ultraviolet, respectively. Foreground field stars and background galaxies were masked before flux extraction (see Gil De Paz et al. 2006). Some of the SINGS galaxies have not yet been observed with GALEX but observations are soon planned (NGC 1377, NGC 3184, NGC 5033, and IC 4710), and a few only have near-ultraviolet observations because the far-ultraviolet detector was turned off at that time (see Table 2). There are a few sources for which there are restrictions (e.g., bright nearby stars) that make it unlikely GALEX will obtain data (NGC 5408 and NGC 6946).

The uncertainties listed in Table 2 include the formal uncertainties from the weighted fits to the growth curves using the uncertainties of the individual points in the growth curves, in addition to absolute calibration uncertainties of ∼15% in both the far- and near-ultraviolet.

[1]A few SINGS sources are not in the *GALEX Atlas of Nearby Galaxies*, but the observing and data reduction procedures for these galaxies are the same as for the *Atlas* targets (e.g., M81 Dwarf A, NGC 3773, NGC 4254, NGC 4725, and NGC 6882).

3.2. Optical Data

The optical imaging for the SINGS project was carried out over the course of five observing runs at the Kitt Peak National Observatory 2.1 m and one observing run at the Cerro Tololo Inter-American Observatory 1.5 m telescopes between March 2001 and February 2003. Broadband photometry was obtained in $BVRI$ using 2K×2K CCDs with pixel scales and fields-of-view of $0\farcs305$ and $10'$ at KPNO and $0\farcs433$ and $14\farcm5$ at CTIO. Galaxies more extended than the CCD fields-of-view were imaged at multiple, overlapping pointings. Typical exposure times were 1440 s (B), 720 s (V), 420 s (R), and 840 s (I), usually split into two separate exposures to aid cosmic ray removal. Such exposures reach a depth of about 25 mag arcsec^{-2} at a signal-to-noise ratio of ∼10.

Data processing consisted of standard routines such as bias subtraction, flat-fielding with both dome- and twilight-flats, cosmic ray removal, and the mosaicking of overlapping pointings for galaxies with large angular extents. The southern $3'$ of the KPNO 2.1 m CCD field-of-view suffers from vignetting; care is taken to remove as much of the vignetted portion of the KPNO images as feasible. Photometric standard stars were observed during each observing run to flux calibrate the images. Most images have photometric accuracy of 5% or better.

Global optical fluxes are extracted using the same apertures used for the IRAC and MIPS global flux extractions; these apertures cover at least the entire optical disk (see Table 1) and are chosen to be large enough to encompass all of the optical and infrared emission. Sky estimation and subtraction is carried out through the use of multiple sky apertures placed near the source without overlapping the faintest isophotes visible from the galaxy. Foreground stars are edited from the optical images after first being conservatively identified using $f_\nu(3.6\ \mu\mathrm{m})/f_\nu(8.0\ \mu\mathrm{m})$ and $f_\nu(8.0\ \mu\mathrm{m})/f_\nu(24\ \mu\mathrm{m})$ color images (e.g., $f_\nu(8.0\ \mu\mathrm{m})/f_\nu(24\ \mu\mathrm{m})_{\mathrm{stellar}} > 8$).

3.3. Radio Data

Global 20 cm continuum fluxes from the literature are available for 62 SINGS galaxies, with data for 51 of these galaxies taken from the New VLA Sky Survey catalog (Condon et al. 1998; Yun, Reddy, & Condon 2001; see Table 3). Although this is a snapshot survey and prone to miss extended emission from galaxies having large angular extents, proper attention has been paid to these effects to derive unbiased 1.4 GHz fluxes (e.g., Yun, Reddy, & Condon 2001). The 20 cm data for 11 additional galaxies derive from Condon (1987), Hummel (1980), Condon et al. (1990), Wright & Otrupcek (1990), Bauer et al. (2000), and Cannon et al. (2006b).

3.4. Infrared Data

A full description of the infrared (2MASS, *ISO*, *IRAS*, *Spitzer*) and submillimeter (SCUBA) data can be found in Dale et al. (2005). In this section we present details of a few additional

modifications and updates to the *Spitzer* data. For example, the MIPS flux calibrations and their uncertainties have been tweaked since Dale et al. (2005)—the 24, 70, and 160 μm fluxes have been respectively boosted by factors 1.018, 1.107, and 1.049, and their systematic uncertainties have dropped to 4, 7, and 12%. The uncertainties provided in Table 3 include both calibration and statistical uncertainties. Calibration uncertainties remain at 10% for IRAC data.

The IRAC flux densities in Table 3 include extended source aperture corrections provided by the Spitzer Science Center[2]. For an effective aperture radius $r = \sqrt{ab}$ in arcseconds derived from the semi-major a and semi-minor b ellipse axes provided in Table 1, the IRAC extended source aperture correction is

$$f^{\rm IRAC}_{\rm true}/f^{\rm IRAC}_{\rm measured} = A{\rm e}^{-r^B} + C, \quad (1)$$

where A, B, and C are listed in Table 4. The average extended source aperture corrections ($\sim$10% uncertain) for the SINGS IRAC photometry are [0.912,0.942,0.805,0.749] at [3.6,4.5,5.8,8.0](μm).

The MIPS flux densities in Table 3 also include extended source aperture corrections. Three high-resolution models of a galaxy's structure are generated by convolving the MIPS PSFs with an R band image of the galaxy. The MIPS aperture corrections listed in Table 5 are computed for the same apertures used in the global flux extractions (Table 1). The median aperture corrections are [1.01,1.04,1.10] at [24,70,160](μm). The uncertainties in the aperture corrections are typically a few percent, and are based on the differences between the canonical and "minimum" corrections. Minimum MIPS aperture corrections are computed assuming point source light distributions.

Finally, a correction for 70 μm non-linearity effects is included in this presentation. A preliminary correction of the form

$$f^{70\mu{\rm m}}_{\rm true} = 0.581(f^{70\mu{\rm m}}_{\rm measured})^{1.13}, \quad (2)$$

derived from data presented by Gordon et al. (2006, in preparation), is applied to pixel values above a threshold of $\sim$66 MJy sr^{-1}. A total of 40 SINGS 70 μm images require such a correction. The median correction to the global 70 μm flux density for these 40 galaxies is a factor of 1.03, with the three largest corrections being factors of 1.124 (NGC 4826), 1.128 (NGC 1482), and 1.158 (NGC 7552).

4. Results

4.1. Global Broadband Spectral Energy Distributions

Figures 1-8 show the ultraviolet-to-submillimeter spectral energy distributions for the SINGS sample. The solid curve is the sum of a dust (dashed) and a stellar (dotted) model. The dust curve is a Dale & Helou (2002) model (least squares) fitted to ratios of the 24, 70, and 160 μm fluxes

[2]See spider.ipac.caltech.edu/staff/jarrett/irac/calibration/

(a dust curve for NGC 3034 is fit using *IRAS* 25, 60, and 100 μm data, since the MIPS data for this galaxy are saturated). The $\alpha_{\rm SED}$ listed within each panel parametrizes the distribution of dust mass as a function of heating intensity, as described in Dale & Helou (2002). The stellar curve is a 1 Gyr continuous star formation, solar metallicity curve from Vazquez & Leitherer (2005) fitted to the 2MASS data. The initial mass function for this curve utilizes a double power law form, with $\alpha_{1,\rm IMF} = 1.3$ for $0.1 < m/M_{\odot} < 0.5$ and $\alpha_{2,\rm IMF} = 2.3$ for $0.5 < m/M_{\odot} < 100$ (e.g., Kroupa 2002). This stellar curve (not adjusted for internal extinction) is included as a "standard" reference against which the deviations in the ultraviolet and optical data, from the stellar curve, can be compared from galaxy to galaxy. The stellar curve also serves to highlight the relative importance of stars and dust in each galaxy, particularly in the transition from stellar to dust emission in the mid-infrared (e.g. NGC 1404 versus NGC 1482).

Several galaxies show mid-infrared data that deviate from the fits. Most of these systems are low metallicity objects (e.g., Ho II, NGC 2915, IC 2574, DDO 154, DDO 165, and NGC 6822), objects that have been shown to be deficient in PAH emission (see the discussion in Section 4.2). The mid-infrared data for NGC 1377 are also quite discrepant from the model, showing a strong excess for each of the broadband filters from 3.6 to 15 μm. The substantial hot dust emission and lack of optical signatures or synchrotron radiation led Roussel et al. (2003) to infer that this heavily extincted system is undergoing the very beginnings of an intense burst of star formation.

4.2. Spectral Energy Distributions Binned by the Infrared-to-Ultraviolet Ratio

Spatially-resolved panchromatic surveys of galaxies at high redshift ($z \gtrsim 1$) are beyond the reach of present technology. Analysis of the distribution of global (spatially-integrated) spectral energy distributions is a sensible starting point for current cosmology surveys (e.g., Rowan-Robinson et al. 2005). Figure 9 shows a stack of SINGS spectral energy distributions that emphasizes the infrared-to-ultraviolet variations within the SINGS sample. Each spectral energy distribution in the stack represents an average of approximately 10 individual spectral energy distributions that fall within a given bin of the total infrared-to-ultraviolet ratio. The ultraviolet emission for this ratio is computed as $\nu f_{\nu}(1500\text{Å}) + \nu f_{\nu}(2300\text{Å})$ whereas the "total infrared" is the dust continuum emission between 3 and 1100 μm (Dale et al. 2001), computed using the MIPS 24, 70, and 160 μm fluxes and Equation 4 of Dale & Helou (2002). The spectra are arbitrarily normalized at the 2MASS $K_{\rm s}$ band wavelength.

Several features in the stack are immediately noticeable. The ultraviolet slopes vary from positive values for galaxies with high infrared-to-ultraviolet ratios to negative values for low infrared-to-ultraviolet ratio galaxies (as will be explored in detail in § 5.5). The 4000Å break shows up quite clearly, even at this coarse spectral "resolution." Other obvious features include: the broad far-infrared peak signifying emission from cool-to-warm large grains; the contributions from polycyclic aromatic hydrocarbons appearing as mid-infrared emission features; and the near-infrared bump arising from photospheric emission from old stellar populations. Note also the broad spread in the

ultraviolet data compared to that in the far-infrared. The variations in the infrared-to-ultraviolet ratio studied later in this work are largely driven by variations in the ultraviolet emission.

Close inspection of Figure 9 reveals that most of the variation in the stacked spectra stem from the two extreme bins (bins "1" and "6") in the infrared-to-ultraviolet ratio. However, substantial variations are still seen in bins 2-5 at ultraviolet and mid-infrared wavelengths. The bin 2-5 spread is 0.88, 0.78, 0.24, and 0.16 dex at 0.15, 0.23, 8.0, and 24 μm (compared to the full spreads of 1.76, 1.46, 0.80, and 0.80 dex over bins 1-6 at the same wavelengths). The spread at ultraviolet wavelengths is presumably significantly affected by variations in dust content. The range in 8.0 μm emission, on the other hand, is likely due to PAH destruction/formation variations. Low metallicity systems, for example, are known to be deficient in PAH emission (e.g., Dale et al. 2005; Engelbracht et al. 2005; Galliano et al. 2005). Indeed, eight of the nine galaxies in the lowest infrared-to-ultraviolet ratio bin have low metallicities ($12 + \log(\mathrm{O/H}) < 8.1$; Moustakas et al. 2006, in preparation), and this bin's average spectrum in Figure 9 shows very low mid-infrared emission. The 24 μm emission from galaxies is known to be sensitive to the star formation rate (e.g., Dale et al. 2005; Gordon et al. 2004; Helou et al. 2004; Hinz et al. 2004; Calzetti et al. 2005); the observed variations at this wavelength may be strongly affected by the range in the sample's star formation properties.

4.3. Principal Component Analysis

A principal component analysis can help to quantify relative contributions to the observed variations in a sample of spectral energy distributions (Deeming 1964). A set of i eigenvectors $\{\vec{e}_i\}$ and their corresponding eigenvalues $\{e_i\}$ for our sample of N galaxies are computed from a diagonalization of the covariance matrix

$$C_{jk} = \frac{1}{N}\Sigma_{i=1}^{N}\, \nu f_\nu^i(\lambda_j)\, \nu f_\nu^i(\lambda_k), \tag{3}$$

where $\nu f_\nu^i(\lambda_j)$ is the flux of the i^{th} spectrum at wavelength λ_j. We restrict the computation of the covariance matrix to involve only those wavelengths for which we have a substantial database of fluxes; submillimeter data at 450 and 850 μm are not included in the principal component analysis. Furthermore, to avoid spurious results we do not include in our analysis any SINGS galaxies without a secure detection/measurement at any of the ultraviolet, optical, near-infrared, or infrared wavelengths listed in Tables 2-3. Hence, our principal component analysis involves only about three-fourths of the SINGS sample (Table 1 indicates which systems are involved). Our principal component analysis is carried out after normalizing the spectra at the 2MASS K_{s} band wavelength.

The two largest eigenvalues e_1 and e_2 correspond to the eigenvectors $\vec{e}_1$ and $\vec{e}_2$ that describe most of the variation in the spectral atlas. Normalizing the eigenvalues by their sum, $e_i' = e_i/\Sigma_j e_j$, shows that $\vec{e}_1$ and $\vec{e}_2$ respectively contribute to 89% and 7% of the observed variation in the sample spectra (i.e., $e_1' = 0.89$ and $e_2' = 0.07$; the remaining normalized eigenvalues are individually

smaller than 0.02). To quantify the uncertainty on these numbers, we have performed 10,000 Monte Carlo simulations of the principal component analysis. For each simulation we use the tabulated flux uncertainties to add a random (Gaussian deviate) flux offset to every galaxy's flux at each wavelength. The means of the two largest normalized eigenvalues from these simulations are $\langle e'_1 \rangle = 0.88 \pm 0.01$ and $\langle e'_2 \rangle = 0.07 \pm 0.01$, with the error bars reflecting the 1σ standard deviation from the simulations. The means of the two primary eigenvectors, $\langle \vec{e}_1 \rangle$ and $\langle \vec{e}_2 \rangle$, are displayed in Figure 10. Eigenvector $\langle \vec{e}_1 \rangle$ is indicative of a galaxy with a low infrared-to-ultraviolet ratio, whereas $\langle \vec{e}_2 \rangle$ represents a high infrared-to-ultraviolet spectrum. The error bars shown in Figure 10 portray the 1σ dispersions for each data point from the simulations.

5. The Infrared-to-Ultraviolet Ratio

The infrared-to-ultraviolet ratio is sensitive to the metal content, star formation history, and the geometry of interstellar grains and their heating sources. The infrared-to-ultraviolet ratio is also a rough measure of the amount of extinction at ultraviolet wavelengths. What is the predominant driver of the variations in this ratio in galaxies? Which parameters can be used to most easily quantify these variations, with the aim of simplifying SED analysis? Various possibilities are presented and discussed below.

5.1. Inclination

The tilt of a spiral disk with respect to the observer's line-of-sight affects the observed intensity and colors (e.g., Bruzual, Magris, & Calvet 1988; Boselli & Gavazzi 1994; Giovanelli et al. 1995; Kuchinski et al. 1998). The "disk" inclination can be computed from the observed semi-major and semi-minor axes, a and b, assuming that disks are oblate spheroids with intrinsic axial ratio $(b/a)_{\rm int}$ using the relation:

$$\cos^2 i = \frac{(b/a)^2 - (b/a)^2_{\rm int}}{1 - (b/a)^2_{\rm int}}, \tag{4}$$

where $(b/a)_{\rm int} \simeq 0.2$ for morphological types earlier than Sbc and $(b/a)_{\rm int} \simeq 0.13$ otherwise (see Dale et al. 1997 and references therein). Figure 11 gives the infrared-to-ultraviolet ratio as a function of galaxy disk inclination. Galaxies with elliptical and irregular morphologies have not been included in the plot. The (arbitrarily normalized) dotted line shows the expected effect of extinction on the ultraviolet data with changing inclination using the thin disk model and a central face-on optical depth in the B band of $\tau_B^{\rm f} = 2$ described in Tuffs et al. (2004). The ratio does not obviously trend with galaxy orientation; if there is a trend consistent with the model of Tuffs et al., it is a weak trend that is washed out by a large dispersion. The data in Figure 11 indicate that moderate disk inclinations are not a dominant factor in determining the infrared-to-ultraviolet ratio in SINGS galaxies.

5.2. Hubble Type

Figure 12 displays the infrared-to-ultraviolet ratio as a function of galaxy optical morphology. In general, the ultraviolet light increases in importance as the morphology changes from early-type spirals to late-type spirals to irregulars, reflecting the changing significance of star formation and the ultraviolet luminosity to the overall energy budget in galaxies. However, elliptical and S0 galaxies do not follow this general trend; some ellipticals and S0s show comparatively low infrared-to-ultraviolet ratios. This deviation to low infrared-to-ultraviolet ratios for some of the earliest-type galaxies is due excess to an excess of observed ultraviolet emission, or alternatively, due to a relative paucity of ultraviolet photons captured by dust grains and reprocessed as infrared radiation; the infrared portion of the bolometric luminosity in ellipticals is typically only a few percent (Xilouris et al. 2004). Moreover, some elliptical systems are conspicuous ultraviolet emitters, with the emission thought to mainly arise from low-mass, helium-burning stars from the extreme horizontal branch and later phases of stellar evolution (see O'Connell 1999 for a review). Low or moderate levels of star formation could also contribute to the ultraviolet emission in early-type galaxies (e.g., Fukugita et al. 2004). Recent evidence shows that strong ultraviolet emitters are the largest contributers to the significant scatter in the ultraviolet colors of early-type galaxies (e.g., Yi et al. 2005; Rich et al. 2005).

This wide range in the fractional ultraviolet luminosity also leads to significant scatter in the infrared-to-ultraviolet ratio. Though the statistics are based on small numbers, a similarly large dispersion is seen for irregular systems at the other end of the morphological spectrum. Part of this dispersion is likely associated with the metal content in irregular/dwarf systems. In general, irregular galaxies are quite blue and metal-poor (e.g., Hunter & Gallagher 1986; van Zee, Haynes, & Salzer 1997). Ultraviolet/optical continuum emission from low-metallicity galaxies experiences less extinction, which starves the production of infrared continuum emission (see previous paragraph). The combination of these effects leads to lower infrared-to-ultraviolet ratios.

5.3. Far-Infrared Color

Though dwarf irregulars show low infrared-to-ultraviolet ratios, their interstellar dust grains tend to be vigorously heated. The lower metallicity in these systems results in less line blanketing which in turn leads to harder radiation fields. Many of the dwarf and irregular systems in the SINGS sample indeed have elevated $f_\nu(70\mu\mathrm{m})/f_\nu(160\mu\mathrm{m})$ ratios (e.g., Dale et al. 2005; Walter et al. 2006), indicating strong overall heating of the dust grain population. The warmer far-infrared colors for SINGS dwarfs/irregulars are shown in Figure 13.

An interesting feature to this plot is the apparent wedge-shaped distribution, with a progressively smaller range in the infrared-to-ultraviolet ratio for cooler far-infrared colors. There is no obvious trend in infrared-to-ultraviolet ratio with disk inclination (Figure 11), so it is unlikely that the distribution in Figure 13 is due solely to disk orientation. However, geometry may play a key

role in creating this distribution. Perhaps galaxies with relatively high $f_\nu(70\mu\mathrm{m})/f_\nu(160\mu\mathrm{m})$ ratios have hotter dust since the dust in such systems is near sites of active star formation or active nuclei. Moreover, galaxies that appear as several bright clumps in the infrared provide a large number of low optical depth lines-of-sight from which ultraviolet photons may escape (or their ultraviolet emission does not come from a temporally singular event, but is rather more continuous or multi-generational in nature). Such clumpy galaxies would hence show comparatively low infrared-to-ultraviolet ratios. On the other hand, ultraviolet photons from galaxies that appear in the infrared as a single point-like blob of nuclear emission would encounter significant extinction, and hence such galaxies would exhibit high infrared-to-ultraviolet ratios. In contrast to hot dust systems, galaxies with relatively low $f_\nu(70\mu\mathrm{m})/f_\nu(160\mu\mathrm{m})$ ratios have cooler dust because the dust is not in spatial proximity of the hot stars (e.g., Panagia 1973). The heating of dust via the weaker ambient interstellar radiation field would be fractionally higher in these galaxies. Therefore, their morphological appearance in the infrared should be comparatively smooth.

Since the relative distribution of interstellar grains and their heating sources is central to the scenario outlined above, we turn to the 24 μm morphology of SINGS galaxies to provide a test of the above scenario. MIPS 24 μm data may be uniquely suited for such a test, as the data have significantly higher spatial resolution than either 70 or 160 μm imaging, and effectively trace both interstellar grains and active sites of star formation (e.g., Hinz et al. 2004; Gordon et al. 2004). In fact, the 24 μm emission can be spatially closely associated with H II regions, and in such cases is probably dominated by dust from *within* these regions (Helou et al. 2004). Point source photometry is done using StarFinder (Diolaiti et al. 2000), which is appropriate for the stable and well sampled MIPS 24 μm PSF. A STinyTim (Krist 2002) model PSF with a temperature of 100 K, smoothed to account for pixel sampling, is used. Smoothed STinyTim PSFs are excellent matches to observed MIPS 24 μm PSFs (Engelbracht et al. 2006, in preparation). An image of all the detected point sources is created along with a difference image made by subtracting the point source image from the observed image. The fluxes are measured in the point source ("unresolved") and difference ("resolved") images in the same aperture used for the total galaxy measurement (see Figure 14). In addition, nuclear fluxes are measured in a $12''$ radius circular aperture on the observed image.

The results from this analysis are displayed in Figures 15 and 16. In Figure 15 the symbol size linearly scales with the ratio of nuclear-to-total 24 μm emission, with the largest symbols corresponding to ratios $\sim$0.9. In addition, listed near each data point is the ratio of resolved-to-unresolved 24 μm emission. Galaxies dominated by a single point source of nuclear emission at 24 μm (i.e., large symbols) appear preferentially in the upper righthand portion of the diagram. These galaxies contain hot dust and show relatively high infrared-to-ultraviolet ratios since the dust is centrally concentrated near the heating sources in the nuclei. Note that nuclear activity is not the main factor in determining the 24 μm morphology—only two of the point-like systems have active nuclei (NGC 1266 and NGC 5195). Systems with clumpy 24 μm morphologies appearing in the lower righthand corner show smaller nuclear-to-total ratios (smaller symbol sizes), but still contain hot dust; the dust is concentrated around several heating sources, not just the nuclear ones.

Moreover, the clumpy distribution provides a larger number of low τ or 'clean' lines-of-sight for ultraviolet photons to escape the galaxies, leading to lower infrared-to-ultraviolet ratios. Finally, galaxies with smoother 24 μm morphologies (small symbol sizes and high resolved-to-unresolved ratios) exhibit lower far-infrared colors. To see this latter effect more clearly, we show in Figure 16 the ratio of resolved-to-unresolved 24 μm emission as a function of far-infrared color. Clearly there is a trend, indicating that the 24 μm morphology can, for nearby galaxies, indicate the relative separation between interstellar grains and their heating sources. Note that distance is not a driving factor in this trend (the symbol sizes are scaled according to galaxy distance). In short, the 24 μm morphology data support the scenario described in the previous two paragraphs.

5.4. Specific Star Formation Rate

One way to parametrize the star formation formation history of a galaxy is via the star formation rate per stellar mass, or the specific star formation rate (SSFR). Drory et al. (2004) and Feulner et al. (2005), for example, have utilized the specific star formation rate to explore the role of star formation in the growth of stellar mass over cosmic timescales. In this work the specific star formation rate is quantified as

$$\mathrm{SSFR}\ [\mathrm{yr}^{-1}] = (\ 4.5\mathrm{TIR}[10^{37}\mathrm{W}] + 7.1\nu L_{\nu}(1500\mathring{A})[10^{37}\mathrm{W}]\ )\ /\ \nu L_{\nu}(K_{\mathrm{s}})[L_{\odot}] \qquad (5)$$

based on star formation rate conversion factors from Kennicutt (1998). The numerator in Equation 5 is a more robust way to quantify the star formation rate than relations that are limited to either infrared or ultraviolet luminosities. The infrared luminosity accurately corresponds to the star formation rate only in the limiting case where all the star formation-related stellar emission is captured by interstellar dust grains. Similarly, the ultraviolet emission can also be a poor measure of the star formation rate, especially when extinction is significant. However, combining both the ultraviolet and infrared luminosities in Equation 5 is akin to an extinction-corrected ultraviolet luminosity and thus more effectively recovers the true star formation rate (see also Bell 2003 and Iglesias-Páramo et al. 2006). The K_{s} band luminosity in the denominator of Equation 5 is equivalent to a stellar mass; Bell et al. (2003), for example, fit stellar population synthesis models to thousands of 2MASS plus Sloan Digital Sky Survey optical-near-infrared datasets and find the distribution of $M_{*}/L_{K\mathrm{s}}$ peaks near $\sim 0.8\ M_{\odot}/L_{\odot}$ for a wide range of galaxy masses.

Figure 17 presents the interplay between the specific star formation rate, the infrared-to-ultraviolet ratio, and optical morphology. With the exception of a handful of high infrared-to-ultraviolet sources known to be unresolved at 24 μm, the SINGS sample shows a general trend in this diagram. Galaxies with low specific star formation rates ($\mathrm{SSFR}\lesssim 0.9\ \mathrm{yr}^{-1}$) are of E, S0, S0/a, or Sa morphologies, consistent with the traditional notion that early-type galaxies exhibit low star formation rates per unit stellar mass. These early-type galaxies show increasing infrared-to-ultraviolet ratios for increasing specific star formation rates. In contrast, spiral galaxies generally show $\mathrm{SSFR}\gtrsim 0.9\ \mathrm{yr}^{-1}$, and the later the spiral Hubble type the larger the specific star formation

rate and the smaller the infrared-to-ultraviolet ratio.

Perhaps this overall trend is related to the geometry argument presented in Section 5.3. Compared to late-type galaxies, early-type systems typically have twice the ratio of resolved-to-unresolved 24 μm emission. Thus, increasing the specific star formation rate in early-type systems serves to increase the infrared-to-ultraviolet ratio, as the additional ultraviolet photons are relatively easily captured by the distributed population of interstellar dust grains and converted to infrared light. On the other hand, increasing the specific star formation rate in late-type galaxies results in smaller infrared-to-ultraviolet ratios—the additional ultraviolet photons in spirals with high SSFRs tend to more easily escape the galaxies, since their clumpy distribution of dust provides many more sightlines of low optical depth than found in 24 μm-smooth early-types.

5.5. Ultraviolet Spectral Slope

The infrared-to-ultraviolet ratio has been shown to be fairly tightly correlated with the ultraviolet spectral slope in starburst galaxies, an important discovery that allows the extinction at ultraviolet wavelengths to be estimated from ultraviolet spectral data (e.g., Calzetti, Kinney, & Storchi-Bergmann 1994; Calzetti 1997; Meurer, Heckman, & Calzetti 1999). Non-starbursting galaxies have also been studied in this context, but their data show a larger dispersion, with normal star-forming and quiescent systems exhibiting redder ultraviolet spectra and/or lower infrared-to-ultraviolet ratios (e.g., Buat et al. 2002; Bell 2002; Kong et al. 2004; Gordon et al. 2004; Buat et al. 2005; Calzetti et al. 2005; Seibert et al. 2005; Cortese et al. 2006; Boissier et al. 2006; Gil de Paz et al. 2006). The intrinsic ultraviolet spectral slope is quite sensitive to the effective age of the stellar population, leading Calzetti et al. (2005) to suggest that the evolved, non-ionizing stellar population ($\sim$50-100 Myr) dominates the ultraviolet emission in normal systems, in contrast to current star formation processes dominating the ultraviolet emission in starbursts. The increased diversity in the ultraviolet spectral slopes for evolved stellar populations manifests itself as an increased dispersion for quiescent and normal star-forming galaxies in plots of the infrared-to-ultraviolet ratio as a function of ultraviolet spectral slope. Interestingly, Boissier et al. (2006) use azimuthally-averaged radial profiles, and after excluding emission from the bulge/nucleus, they find the relation between infrared-to-ultraviolet and ultraviolet slope tightens up compared with the one obtained using the integrated data. This result is consistent with the interpretation of Calzetti et al. if the evolved stellar populations in normal star-forming galaxy bulges cause the increased scatter compared to the starburst trend.

Figure 18 displays such a diagram for this study. Normal star-forming and starbursting galaxies from Kong et al. (2004) and Calzetti et al. (1995) are plotted in addition to the SINGS data points. The dotted curve is that for starbursting galaxies from Kong et al. (2004) and the solid curve is applicable to normal star-forming galaxies (Cortese et al. 2006). Similar to what has been found for other samples of non-starbursting galaxies, the SINGS dataset shows more scatter in this diagram and the galaxies are redder in their ultraviolet spectral slope compared to starburst

galaxies. Inspection of the distribution as a function of SINGS optical morphology, however, shows that the 14 reddest SINGS galaxies are type Sab or earlier; the early-type galaxies in SINGS contribute to most of the observed scatter.

6. Discussion and Summary

The ultraviolet-to-radio broadband spectral energy distributions are presented for the 75 galaxies in the *Spitzer* Infrared Nearby Galaxies Survey, a collection of galaxies that broadly samples the wide variety of galaxy morphologies, luminosities, colors, and metallicities seen in the Local Universe. The infrared-to-ultraviolet ratio is explored in conjunction with several global parameters. An interesting empirical finding is that systems with cooler dust show a restricted range of infrared-to-ultraviolet ratios ($\sim$0.5 dex), while systems with warm global far-infrared colors exhibit a large range of infrared-to-ultraviolet ratios ($\sim$3 dex). We use the morphology from MIPS 24 μm imaging to interpret this distribution to result from the relative geometry of dust grains and their heating sources. Nearby galaxies with globally cooler dust appear smoother at 24 μm, from which we infer that the dust grains are well mixed throughout the interstellar medium and not concentrated near sites of active star formation. On the other hand, galaxies with elevated $f_\nu(70\mu\mathrm{m})/f_\nu(160\mu\mathrm{m})$ ratios appear as one or a handful of clumps at 24 μm and thus have much of their dust considerably closer to heating sources. The observed range in infrared-to-ultraviolet ratio is also related to the 24 μm morphology, from which the density of available clean lines-of-sight for ultraviolet photons to escape can be inferred. The dust distribution in galaxies appearing as a single clump at 24 μm heavily enshrouds the heating sources (high infrared-to-ultraviolet ratios), galaxies with multiple clumps at 24 μm provide a large number of low optical depth lines-of-sight along which ultraviolet photons can escape (low infrared-to-ultraviolet ratios), and a smooth distribution at 24 μm implies a dust distribution that provides an intermediate number of low optical depth lines-of-sight (average infrared-to-ultraviolet ratios). Detailed studies of the relative distributions of the infrared emission and the ionizing radiation fields in SINGS galaxies have been carried out in IC 2574 (Cannon et al. 2005), NGC 1705 (Cannon et al. 2006a), and NGC 6822 (Cannon et al. 2006b). These dwarf galaxies appear as multiple clumps at 24 μm and show low optical extinctions and highly variable ratios of Hα-to-infrared (i.e., significant ultraviolet photon leakage), consistent with our expectation that multi-clump 24 μm galaxies should have warm far-infrared colors and low infrared-to-ultraviolet ratios.

In a study of 99,088 galaxies from the Sloan Digital Sky Survey, Obrić et al. (2006) find that the GALEX, Sloan, and 2MASS data "form a nearly one parameter family." In particular, they can predict with 20% accuracy the 2MASS K_s flux using just the Sloan u and r fluxes. In addition, they can predict to within a factor of two certainty the *IRAS* 60 μm flux based on the Sloan broadband data. Such simple optical-infrared correlations are not seen for SINGS galaxies. However, Obrić et al. are only able to identify *IRAS* fluxes for less than 2% of their sample, and this subset is strongly biased to optically blue galaxies. The SINGS sample, though far smaller in size, provides

complete panchromatic information for a far more diverse ensemble of galaxies and is thus much less biased to a particular subset of the local galaxy population.

A principal component analysis of the SINGS broadband spectra indicates that most of the sample's large broadband spectral variations stem from two underlying components, one typical of a galaxy with a low infrared-to-ultraviolet ratio (88% of the sample variation) and one indicative of a galaxy with a high infrared-to-ultraviolet ratio (7% of the sample variation). From a morphological standpoint, we find that much of the dispersion in plots such as infrared-to-ultraviolet versus ultraviolet spectral slope (Figure 18) stems from early-type galaxies, which have significantly redder ultraviolet spectra than other galaxy types. In fact, the galaxies with the highest optical-to-infrared ratios, the smallest specific star formation rates, and the reddest ultraviolet slopes are all early-type galaxies (see Figures 1-8, 17, and 18, respectively). The implication is that the star formation history (i.e., the specific star formation rate, the birthrate parameter or some other measure of the current-to-past star formation rate) may be the dominant regulator of the broadband spectral variations between galaxies.

Support for this work, part of the *Spitzer Space Telescope* Legacy Science Program, was provided by NASA through Contract Number 1224769 issued by the Jet Propulsion Laboratory, California Institute of Technology under NASA contract 1407. AGdP is financed by the MAGPOP EU Marie Curie Research Training Network and the Spanish Programa Nacional de Astronomía y Astrofísica under grant AYA2003-01676. We are thankful for the hard work put in by the instrument teams and the *Spitzer* Science Center. We gratefully acknowledge NASA's support for construction, operation, and science analysis for the GALEX mission, developed in cooperation with the Centre National d'Etudes Spatiales of France and the Korean Ministry of Science and Technology. This research has made use of the NASA/IPAC Extragalactic Database which is operated by JPL/Caltech, under contract with NASA. This publication makes use of data products from the Two Micron All Sky Survey, which is a joint project of the University of Massachusetts and IPAC/Caltech, funded by NASA and the National Science Foundation.

REFERENCES

Adelberger, K.L. & Steidel, C.C. 2000, ApJ, 544, 218

Bauer, F.E., Condon, J.J., Thuan, T.X., & Broderick, J.J. 2000, ApJS, 129, 547

Bell, E.F. 2002, ApJ, 577, 150

Bell, E.F., Gordon, K.D., Kennicutt, R.C., & Zaritsky, D. 2002, ApJ, 565, 994

Bell, E.F. 2003, ApJ, 586, 794

Boissier, S. et al. 2006, ApJ, submitted

Boselli, A., & Gavazzi, G. 1994, A&A, 283, 12

Bruzual A., G., Magris, G., & Calvet, N. 1998, ApJ, 333, 673

Buat, V., Boselli, A., Gavazzi, G., & Bonfanti, C. 2002, A&A, 383, 801

Buat, V. et al. 2005, ApJ, 619, L51

Calzetti, D., Kinney, A.L., Storchi-Bergmann, T. 1994, ApJ, 429, 582

Calzetti, D., Bohlin, R.C., Kinney, A.L., Storchi-Bergmann, T., & Heckman, T.M. 1995, ApJ, 443, 136

Calzetti, D. 1997, AJ, 113, 162

Calzetti, D. et al. 2005, ApJ, 633, 871

Cannon, J.M. et al. 2005, ApJ, 630, L37

Cannon, J.M. et al. 2006a, ApJ, in press

Cannon, J.M. et al. 2006b, ApJ, submitted

Chapman, S.C., Smail, I., Ivison, R.J., Helou, G., Dale, D.A., & Lagache, G. 2002, ApJ, 573, 66

Condon, J.J. 1987, ApJS, 65, 485

Condon, J.J., Helou, G., Sanders, D.B., & Soifer, B.T. 1990, ApJS, 73, 359

Condon, J.J., Cotton, W.D., Greisen, E.W., Yin, Q.F., Perley, R.A., Taylor, G.B., & Broderick, J.J. 1998, AJ, 115, 1693

Cortese, L., Boselli, A., Buat, V., Gavazzi, G., Boissier, S., Gil de Paz, A., Seibert, M., Madore, B.F., & Martin, C. 2006, ApJ, 637, 242

Dale, D.A., Giovanelli, R., Haynes, M.P., Scodeggio, M., Hardy, E., & Campusano, L.E. 1997, AJ, 114, 455

Dale, D.A., Helou, G., Contursi, A., Silbermann, N.A., & Kolhatkar, S. 2001, ApJ, 549, 215

Dale, D.A. & Helou, G. 2002, ApJ, 576, 159

Dale, D.A. et al. 2005, ApJ, 633, 857

de Vaucouleurs, G., de Vaucouleurs, A., Corwin, H.G., Buta, R.J., Paturel, G. & Fouqué, P. 1991, *Third Reference Catalogue of Bright Galaxies* (New York: Springer)

Deeming, T.F. 1964, MNRAS, 127, 493

Diolaiti, E., Bendinelli, O., Bonaccini, D., Close, L., Currie, D., & Parmeggiani, G. 2000, A&AS, 147, 335

Draine, B.T. 2003, ARA&A, 41, 241

Drory, N., Bender, R., Feulner, G., Hopp, U., Maraston, C., Snigula, J., & Hill, G.J. 2004, ApJ, 608, 742

Engelbracht, C.W., Gordon, K.D., Rieke, G.H., Werner, M.W., Dale, D.A., & Latter, W.B. 2005, ApJ, 628, L29

Feulner, G., Goranova, Y., Drory, N., Hopp, U., & Bender, R. 2005, MNRAS, 358, L1

Fukugita, M., Nakamura, O., Turner, E.L., Helmboldt, J., & Nichol, R.C. 2004, ApJ, 601, L127

Galliano, F., Madden, S.C., Jones, A.P., Wilson, C.D., & Bernard, J.P. 2005, A&A, 434, 867

Gil de Paz, A. et al. 2006, ApJ, in press

Giovanelli, R., Haynes, M.P., Salzer, J.J., Wegner, G., da Costa, L.N., & Freudling, W. 1995, AJ, 110, 1059

Gordon, K.D., Clayton, G.C., Witt, A.N., & Misselt, K.A. 2000, ApJ, 533, 236

Gordon, K. et al. 2004, ApJS, 154, 215

Helou, G. et al. 2004, ApJS, 154, 253

Hinz, et al. 2004, ApJS, 154, 259

Hummel, E. 1980, A&AS, 41, 151

Hunter, D.A. & Gallager, J.S. 1986, PASP, 98, 5

Iglesias-Páramo, J. et al. 2006, ApJ, in press

Jarret, T.H., Chester, T., Cutri, R., Schneider, S.E., & Huchra, J.P. 2003, AJ, 125, 525

Kennicutt, R.C. 1998, ARA&A, 36, 189

Kennicutt, R.C. et al. 2003, PASP, 115, 928

Krist, J. 2002, *Tiny Tim/SIRTF User's Guide* (Pasadena: Spitzer Science Center)

Kroupa, P. 2002, Science, 295, 82

Kong, X., Charlot, S., Brinchmann, J., & Fall, S.M. 2004, MNRAS, 349, 769

Kuchinski, L.E., Terndrup, D.M., Gordon, K.D., & Witt, A.N. 1998, AJ, 115, 1438

Li, A. & Draine, B.T. 2001, ApJ, 554, 778

Martin, D.C. et al. 2005, ApJ, 619, L1

Meurer, G.R., Heckman, T.M., & Calzetti, D. 1999, ApJ, 521, 64

Obrić, M. et al. 2006, MNRAS, in press

O'Connell, R.W. 1999, ARA&A, 37, 603

Panagia, N. 1973, AJ, 78, 9

Rich, R.M. et al. 2005, ApJ, 619, L107

Roussel, H., Helou, G., Beck, R., Condon, J.J., Bosma, A., Matthews, K., & Jarrett, T.H. 2003, ApJ, 593, 733

Rowan-Robinson, M. et al. 2005, AJ, 129, 1183

Sajina, A., Scott, D., Dennefeld, M., Dole, H., Lacy, M., & Lagache, G. 2006, MNRAS, in press

Schlegel, D.J., Finkbeiner, D.P., & Davis, M. 1998, ApJ, 500, 525

Schmitt, H.R., Calzetti, D., Armus, L., Giavalisco, M., Heckman, T.M., Kennicutt, R.C., Leitherer, C., & Meurer, G.R. 2006, ApJ, in press

Seibert, M. et al. 2005, ApJ, 619, L55

Tuffs, R.J., Popescu, C.C., Völk, H.J., Kylafis, N.D., & Dopita, M.A. 2004, A&A, 419, 821

van Zee, L., Haynes, M.P., & Salzer, J.J. 1997, AJ, 114, 2479

Vazquez, G.A. & Leitherer, C. 2005, ApJ, 621, 695

Walter, F. et al. 2006, ApJ, submitted

Wright, A. & Otrupcek, R. 1990, Parkes Catalogue, Australian Telescope National Facility

Xilouris, E.M., Madden, S.C., Galliano, F., Vigroux, L., & Sauvage, M. 2004, A&A, 416, 41

Yi, S.K. et al. 2005, ApJ, 619, L111

Yun, M.S., Reddy, N.A., & Condon, J.J. 2001, ApJ, 554, 803

Table 1. Galaxy Data

Galaxy	Optical Morph.	α_0 & δ_0 (J2000)	$2a$ ($''$)	$2b$ ($''$)	PA ($^\circ$)	$f_\nu(24)$[res]/ $f_\nu(24)$[unres][a]	$f_\nu(24)$[nuc]/ $f_\nu(24)$[total][a]
NGC 0024†	SAc	000955.9−245755	301	216	135	...	...
NGC 0337†	SBd	005950.7−073444	253	194	50	1.07	0.17
NGC 0584†	E4	013120.6−065205	326	278	330	2.04	0.39
NGC 0628†	SAc	013641.8+154717	721	717	248	1.19	0.01
NGC 0855	E	021403.9+275239	190	170	338	0.42	0.69
NGC 0925†	SABd	022713.6+333504	735	486	15	1.41	0.02
NGC 1097†	SBb	024618.0−301642	758	612	40	1.57	0.12
NGC 1266†	SB0	031600.7−022541	232	234	0	0.10	0.87
NGC 1291†	SB0/a	031719.1−410632	803	840	0	2.07	0.21
NGC 1316†	SAB0	032241.2−371210	583	864	230	1.67	0.05
NGC 1377	S0	033639.0−205408	181	162	0	0.04	0.85
NGC 1404	E1	033852.3−353540	524	369	239	1.75	0.29
NGC 1482†	SA0	035439.0−203009	349	310	29	0.19	0.77
NGC 1512†	SBab	040355.0−432044	491	287	325	3.03	0.10
NGC 1566†	SABbc	042000.4−545615	435	552	40	0.82	0.11
NGC 1705†	SA0	045413.5−532137	167	120	130	0.97	0.43
NGC 2403†	SABcd	073655.0+653554	1164	848	40	1.32	0.01
Holmberg II†	Im	081906.8+704309	441	430	0	0.60	0.01
M81 Dwarf A	I?	082356.0+710145	78	78	0	...	...
DDO 053†	Im	083406.8+661036	133	110	30	0.13	0.08
NGC 2798†	SBa	091723.1+415957	235	232	0	0.00	0.75
NGC 2841†	SAb	092203.3+505837	342	550	150	4.57	0.04
NGC 2915†	I0	092609.4−763736	132	183	290	0.64	0.53
Holmberg I†	IABm	094030.5+711033	265	228	120	...	...
NGC 2976†	SAc	094715.3+675507	311	457	322	0.89	0.05
NGC 3049	SBab	095449.6+091614	218	160	119	0.17	0.74
NGC 3031	SAab	095531.8+690403	1122	1628	154	1.92	0.07
Holmberg IX	Im	095729.2+690250	247	180	130	...	...
M81 Dwarf B†	Im	100531.3+702152	69	107	140	0.62	0.50
NGC 3190†	SAap	101805.7+214957	196	334	117	0.63	0.35
NGC 3184	SABcd	101815.6+412542	538	614	349	1.37	0.01
NGC 3198†	SBc	101954.8+453301	518	315	125	0.76	0.34
IC 2574†	SABm	102822.7+682448	827	376	140	0.98	0.03
NGC 3265†	E	103106.8+284751	184	175	320	0.12	0.82
Markarian 33†	Im	103231.2+542359	177	181	0	0.12	0.75
NGC 3351†	SBb	104357.5+114219	457	586	10	0.55	0.46
NGC 3521†	SABbc	110548.7−000222	494	766	342	2.82	0.04

Note. — The ellipse parameters used in extracting optical and infrared fluxes are listed above. The position angle is measured east of north.

Note. — †Used in the principal component analysis (see Section 4.3).

[a]See Section 5.3.

Table 1. Galaxy Data (continued)

Galaxy	Optical Morph.	α_0 & δ_0 (J2000)	$2a$ ($''$)	$2b$ ($''$)	PA ($^\circ$)	$f_\nu(24)$[res]/ $f_\nu(24)$[unres][a]	$f_\nu(24)$[nuc]/ $f_\nu(24)$[total][a]
NGC 3621	SAd	111816.1−324835	506	670	0	1.79	0.02
NGC 3627	SABb	112013.4+125927	486	745	347	1.11	0.01
NGC 3773	SA0	113813.1+120644	96	94	0	0.11	0.85
NGC 3938	SAc	115250.3+440715	468	504	0	1.72	0.04
NGC 4125	E6p	120805.8+651024	228	151	0	1.80	0.40
NGC 4236	SBdm	121635.9+692808	420	1129	155	0.52	0.004
NGC 4254	SAc	121849.7+142519	519	420	330	2.10	0.03
NGC 4321	SABbc	122254.8+154907	558	483	310	3.44	0.09
NGC 4450	SAab	122830.1+170454	284	401	0	1.63	0.08
NGC 4536	SABbc	123427.5+021113	454	376	30	0.29	0.48
NGC 4552	E	123539.8+123323	306	306	0	1.61	0.52
NGC 4559	SABcd	123558.1+275752	576	327	50	1.21	0.04
NGC 4569	SABab	123650.2+131001	327	593	21	0.77	0.10
NGC 4579	SABb	123743.6+114900	295	229	0	0.84	0.27
NGC 4594	SAa	123959.4−113714	554	232	0	5.23	0.15
NGC 4625	SABmp	124152.3+411618	190	198	140	1.82	0.21
NGC 4631	SBd	124203.7+323205	952	539	350	2.20	0.03
NGC 4725	SABab	125027.7+252948	523	689	30	1.95	0.01
NGC 4736	SAab	125056.7+410706	1033	824	10	1.53	0.07
DDO 154	IBm	125405.2+270854	198	126	123	0.86	0.00
NGC 4826	SAab	125642.8+214050	448	722	112	3.09	0.14
DDO 165	Im	130625.0+674226	267	150	0	···	0.05
NGC 5033	SAc	131328.2+363534	467	729	0	2.76	0.12
NGC 5055	SAbc	131548.3+420142	893	682	11	2.61	0.04
NGC 5194	SABbc	132950.6+471307	1699	1129	285	1.64	0.002
NGC 5195	SB0p	132959.4+471556	191	202	0	···	···
Tololo 89	SBdm	140121.3−330401	130	196	0	0.13	0.09
NGC 5408	IBm	140321.1−412241	209	256	67	0.28	0.02
NGC 5474	SAcd	140459.9+533913	386	335	120	1.48	0.04
NGC 5713	SABbcp	144011.2−001726	140	153	0	0.57	0.49
NGC 5866	S0	150628.8+554551	500	306	39	0.71	0.34
IC 4710	SBm	182838.9−665903	313	219	30	···	···
NGC 6822	IBm	194453.2−144811	1100	1453	330	···	···
NGC 6946	SABcd	203452.0+600915	818	763	0	1.05	0.23
NGC 7331	SAb	223704.3+342435	683	335	78	3.35	0.06
NGC 7552	SAc	231610.8−423505	441	325	30	0.63	0.72
NGC 7793	SAd	235750.4−323530	754	498	0	1.49	0.03

Note. — The ellipse parameters used in extracting optical and infrared fluxes are listed above. The position angle is measured east of north.

Note. — [†]Used in the principal component analysis (see Section 4.3).

[a]See Section 5.3.

Table 2. Ultraviolet, Optical, and Near-Infrared Flux Densities

Galaxy	E(B-V) (mag)	FUV 1528Å (mJy)	NUV 2271Å (mJy)	B 0.45 μm (Jy)	V 0.55 μm (Jy)	R 0.66 μm (Jy)	I 0.81 μm (Jy)	J 1.25 μm (Jy)	H 1.65 μm (Jy)	K_s 2.17 μm (Jy)
NGC 0024	0.020	8.76 ±1.21	11.43 ±1.58	0.082	0.11	0.11	0.097	0.23	0.25	0.19
NGC 0337	0.112	10.46 ±1.45	18.69 ±2.59	0.11	0.12	0.10	0.085	0.20	0.20	0.17
NGC 0584	0.042	0.37 ±0.05	2.00 ±0.28	0.14	0.28	0.28	0.29	0.91	1.12	0.87
NGC 0628	0.070	75.96 ±10.52	99.23 ±13.74	0.65	0.84	0.76	0.65	1.66	1.67	1.32
NGC 0855	0.071	1.81 ±0.25	3.25 ±0.45	0.034[b]	0.047[b]	···	···	0.096	0.10	0.085
NGC 0925	0.076	50.99 ±7.06	62.43 ±8.65	0.35	0.48	0.59	0.62	0.60	0.65	0.51
NGC 1097	0.027	36.26 ±5.19	50.97 ±7.18	0.51	0.84	0.79	0.82	2.40	2.74	2.29
NGC 1266	0.098	0.049±0.007	0.29 ±0.04	0.020	0.036	0.037	0.035	0.12	0.13	0.12
NGC 1291	0.013	7.38 ±1.02	16.28 ±2.26	0.76	1.48	1.37	1.48	4.34	4.48	3.93
NGC 1316	0.021	3.13 ±0.44	16.58 ±2.30	0.79	1.61	1.58	1.73	4.69	4.90	4.21
NGC 1377	0.028	···	···	0.012	0.023	0.021	0.033	0.10	0.11	0.095
NGC 1404	0.011	0.97 ±0.13	2.76 ±0.38	0.24	0.48	0.48	0.49	1.38	1.59	1.35
NGC 1482	0.040	0.41 ±0.06	1.43 ±0.21	0.024	0.046	0.053	0.052	0.23	0.30	0.29
NGC 1512	0.011	14.95 ±2.08	19.88 ±2.77	0.13	0.25	0.26	0.21	0.81	0.86	0.73
NGC 1566	0.009	54.49 ±7.59	65.52 ±9.07	0.43	0.45	0.47	0.42	1.39	1.42	1.27
NGC 1705	0.008	16.01 ±2.22	16.76 ±2.32	0.037	0.042	0.036	0.028	0.057	0.054	0.044
NGC 2403	0.040	258.11 ±35.74	307.45 ±42.57	1.90	2.42	2.37	3.45	2.94	2.91	2.39
Holmberg II	0.032	47.80 ±6.62	48.23 ±6.68	0.21	0.19	0.25	0.38	0.22	0.34	0.26
M81 Dwarf A	0.020	0.48 ±0.07	0.56 ±0.08	0.002	0.001	0.001	0.002	0.004	0.004	0.003
DDO 053	0.038	2.65 ±0.37	2.58 ±0.36	0.011	0.008	0.006	0.007	0.008	0.014	0.008
NGC 2798	0.020	1.12 ±0.16	2.33 ±0.32	0.059	0.075	0.071	0.089	0.16	0.19	0.17
NGC 2841	0.015	12.99 ±1.80	20.57 ±2.85	0.85	1.00	1.26	1.40	2.81	3.22	2.67
NGC 2915	0.275	16.13 ±2.23	16.43 ±2.27	0.077[b]	0.069	0.071	0.077	0.13	0.15	0.092
Holmberg I	0.050	5.29 ±0.73	5.60 ±0.78	0.032	0.029	0.015	0.021	0.031	0.040	0.016
NGC 2976	0.071	18.86 ±2.61	30.24 ±4.19	0.52	0.47	0.52	0.61	0.86	0.89	0.71
NGC 3049[a]	0.038	···	4.51 ±0.62	0.052	0.051	0.046	0.050	0.078	0.082	0.074
NGC 3031	0.080	178.94 ±24.78	256.33 ±35.49	5.07[b]	8.73[b]	···	···	23.47	25.44	21.29
NGC 3034	0.156	50.08 ±6.93	105.27 ±14.58	3.53	2.79[b]	3.67	4.74	9.24	10.80	10.14
Holmberg IX	0.079	4.01 ±0.56	5.00 ±0.69	0.014	0.010	0.008	0.010	0.025	0.021	0.015
M81 Dwarf B	0.081	0.75 ±0.10	0.92 ±0.13	0.009	0.007	0.007	0.007	0.012	0.014	0.014
NGC 3190	0.025	0.40 ±0.06	1.80 ±0.25	0.21	0.27	0.26	0.37	0.71	0.84	0.74
NGC 3184	0.017	···	···	0.67	0.71	0.70	1.10	1.05	1.14	0.91
NGC 3198	0.012	23.60 ±3.27	28.38 ±3.93	0.21	0.30	0.34	0.42	0.57	0.63	0.55
IC 2574	0.036	46.61 ±6.45	48.37 ±6.70	0.18	0.22	0.20	0.27	0.34	0.23	0.17
NGC 3265	0.024	0.57 ±0.08	0.96 ±0.13	0.021	0.024	0.012	0.024	0.051	0.057	0.048
Markarian 33	0.012	4.13 ±0.57	5.20 ±0.72	0.038	0.034	0.029	0.029	0.049	0.056	0.048
NGC 3351	0.028	17.66 ±2.45	28.77 ±3.98	0.45	0.58	0.71	0.98	1.68	1.77	1.54
NGC 3521	0.057	22.19 ±3.07	44.66 ±6.18	0.89	1.23	1.40	2.32	3.73	4.22	3.50

Note. — See § 3 for corrections that have been applied to the data. The uncertainties include both statistical and systematic effects ($\lesssim$ 10% for the optical and near-infrared data). The 2MASS near-infrared data are from Jarret et al. (2003).

[a]The far-ultraviolet detector was turned off during the observation.

[b]Data from the RC3 catalog (de Vaucouleurs et al. 1991).

Table 2. Ultraviolet, Optical, and Near-Infrared Flux Densities (continued)

Galaxy	E(B-V) (mag)	FUV 1528Å (mJy)	NUV 2271Å (mJy)	B 0.45 μm (Jy)	V 0.55 μm (Jy)	R 0.66 μm (Jy)	I 0.81 μm (Jy)	J 1.25 μm (Jy)	H 1.65 μm (Jy)	K_s 2.17 μm (Jy)
NGC 3621	0.081	76.91 ±11.20	110.23 ±15.76	0.62[b]	1.10	···	1.53	1.94	2.15	1.69
NGC 3627	0.033	30.46 ±4.22	61.43 ±8.51	1.51	1.63	1.51	1.90	3.34	3.73	3.17
NGC 3773	0.027	4.21 ±0.58	5.55 ±0.77	0.036	0.033	0.028	0.031	0.045	0.039	0.037
NGC 3938[a]	0.021	···	36.41 ±5.04	0.44	0.44	0.34	0.41	0.64	0.58	0.54
NGC 4125[a]	0.019	···	3.44 ±0.48	0.49	0.54	0.66	0.87	1.39	1.54	1.29
NGC 4236	0.015	63.45 ±8.79	76.24 ±10.56	0.42	0.53	0.62	0.54	0.63	0.83	0.57
NGC 4254[a]	0.039	···	61.82 ±8.56	0.78	0.75	0.64	0.73	1.27	1.35	1.21
NGC 4321[a]	0.026	···	54.04 ±7.48	0.50	0.70	0.85	1.23	1.87	2.00	1.65
NGC 4450[a]	0.028	···	5.39 ±0.75	0.43	0.53	0.52	0.65	1.20	1.39	1.08
NGC 4536	0.018	16.94 ±2.35	21.93 ±3.04	0.40	0.42	0.47	0.51	0.71	0.75	0.70
NGC 4552	0.041	1.89 ±0.26	4.66 ±0.65	0.37	0.49	0.49	0.58	1.63	1.80	1.46
NGC 4559	0.018	53.79 ±7.45	64.63 ±8.95	0.66	0.50	0.50	0.58	0.77	0.79	0.66
NGC 4569	0.047	6.00 ±0.83	19.69 ±2.73	0.50[b]	0.72[b]	···	···	1.83	2.08	1.67
NGC 4579	0.041	5.85 ±0.81	12.11 ±1.68	0.73	0.76	0.87	1.18	2.05	2.24	1.82
NGC 4594	0.051	5.55 ±0.77	17.72 ±2.47	2.25	2.76	3.41	4.30	8.06	9.19	7.57
NGC 4625	0.018	6.04 ±0.84	7.97 ±1.10	0.073	0.071	0.061	0.071	0.098	0.11	0.089
NGC 4631	0.017	80.95 ±11.21	104.78 ±14.51	1.19	0.91	0.96	1.12	1.75	1.98	1.84
NGC 4725	0.012	22.05 ±3.07	29.61 ±4.13	0.54	0.89	1.04	1.48	2.43	3.18	2.41
NGC 4736	0.018	67.19 ±9.30	91.87 ±12.72	2.50	2.79	2.76	3.39	6.94	7.68	6.44
DDO 154	0.009	4.54 ±0.63	4.42 ±0.61	0.016	0.011	0.009	0.009	0.010	0.012	0.012
NGC 4826	0.041	14.50 ±2.01	37.45 ±5.19	1.41	2.05	···	···	5.67	6.30	5.28
DDO 165	0.024	6.72 ±0.93	8.15 ±1.13	0.041	0.034	0.024	0.023	0.026	0.017	0.010
NGC 5033	0.012	···	···	0.54	0.66	···	0.80	1.21	1.35	1.17
NGC 5055	0.018	39.30 ±5.44	63.42 ±8.78	1.08[b]	1.59[b]	···	···	4.21	4.96	4.05
NGC 5194	0.035	160.03 ±22.16	260.75 ±36.10	1.47	1.96	2.20	3.02	4.99	5.89	4.52
NGC 5195	0.035	3.36 ±0.48	10.04 ±1.40	0.37	0.62	0.81	1.51	2.37	2.80	2.26
Tololo 89	0.066	7.57 ±1.05	11.35 ±1.57	0.078	0.070	0.050	0.060	0.081	0.067	0.054
NGC 5408	0.068	···	···	0.092[b]	0.11[b]	···	···	0.19	0.17	0.11
NGC 5474	0.011	24.35 ±3.37	27.18 ±3.76	0.13	0.17	0.18	0.22	0.14	0.16	0.11
NGC 5713	0.039	5.16 ±0.71	10.02 ±1.39	0.11	0.14	0.16	0.20	0.37	0.39	0.33
NGC 5866	0.013	0.65 ±0.09	4.15 ±0.57	0.48	0.59	0.60	0.73	1.31	1.49	1.26
IC 4710	0.089	···	···	0.10	0.12	0.091	···	0.11	0.10	0.078
NGC 6822	0.231	306.74 ±42.47	401.85 ±56.01	1.58	2.24	1.96	1.49	5.66	5.64	4.26
NGC 6946	0.342	···	···	2.82[b]	4.10	···	5.08	7.27	5.47	5.66
NGC 7331	0.091	15.59 ±2.16	29.70 ±4.11	0.54	0.94	1.09	1.62	2.85	3.36	2.82
NGC 7552	0.014	7.73 ±1.07	15.15 ±2.11	0.17	0.26	0.25	0.23	0.71	0.80	0.70
NGC 7793	0.019	123.99 ±17.17	145.08 ±20.09	0.75	0.92	0.84	0.71	1.68	1.70	1.31

Note. — See § 3 for corrections that have been applied to the data. The uncertainties include both statistical and systematic effects ($\lesssim$ 10% for the optical and near-infrared data). The 2MASS near-infrared data are from Jarret et al. (2003).

[a]The far-ultraviolet detector was turned off during the observation.

[b]Data from the RC3 catalog (de Vaucouleurs et al. 1991).

Table 3. Infrared, Submillimeter, and Radio Flux Densities

Galaxy	3.6 μm (Jy)	4.5 μm (Jy)	5.8 μm (Jy)	8.0 μm (Jy)	24 μm (Jy)	70 μm (Jy)	160 μm (Jy)	450 μm (Jy)	850 μm (Jy)	20 cm (Jy)
NGC 0024	0.10 ±0.01	0.071±0.01	0.089±0.01	0.13 ±0.02	0.13 ±0.01	2.10 ±0.17	7.05 ±0.87	···	···	···
NGC 0337	0.10 ±0.01	0.067±0.009	0.14 ±0.02	0.38 ±0.05	0.66 ±0.03	9.90 ±0.70	19.20 ±2.35	···	0.35±0.05	110 ±11
NGC 0584	0.37 ±0.05	0.22 ±0.03	0.18 ±0.02	0.11 ±0.01	0.051±0.003	0.17 ±0.07	1.07 ±0.39[a]	···	···	<50
NGC 0628	0.87 ±0.12	0.54 ±0.08	1.16 ±0.15	2.70 ±0.34	3.15 ±0.13	32.94 ±2.33	122.40 ±14.72	···	···	173 ±17
NGC 0855	0.043±0.006	0.028±0.004	0.019±0.003	0.046±0.006	0.084±0.004	1.53 ±0.13	2.20 ±0.30	···	···	4.9±0.5
NGC 0925	0.31 ±0.04	0.21 ±0.03	0.35 ±0.04	0.61 ±0.08	0.92 ±0.04	13.52 ±0.98	41.48 ±5.06	···	···	46 ± 5
NGC 1097	1.24 ±0.17	0.80 ±0.11	1.46 ±0.18	3.19 ±0.40	6.52 ±0.26	52.53 ±4.06	151.77 ±18.22	···	1.44±0.78	415 ±42
NGC 1266	0.055±0.008	0.042±0.006	0.057±0.008	0.090±0.012	0.86 ±0.03	11.45 ±0.85	9.59 ±1.17	···	···	116 ±12
NGC 1291	2.11 ±0.29	1.27 ±0.17	0.96 ±0.12	0.64 ±0.08	0.45 ±0.02	5.99 ±0.45	29.88 ±3.68	···	···	···
NGC 1316	2.48 ±0.34	1.53 ±0.21	1.13 ±0.14	0.55 ±0.07	0.37 ±0.02	4.69 ±0.33	10.13 ±1.22	···	···	256 ±26
NGC 1377	0.057±0.008	0.085±0.012	0.27 ±0.04	0.42 ±0.05	1.77 ±0.07	5.58 ±0.41	3.05 ±0.39	···	···	<1.0
NGC 1404	0.73 ±0.10	0.43 ±0.06	0.33 ±0.04	0.16 ±0.02	0.085±0.005	0.16 ±0.09[a]	0.32 ±0.18[a]	···	···	3.9±0.6
NGC 1482	0.21 ±0.03	0.15 ±0.02	0.59 ±0.08	1.56 ±0.19	3.67 ±0.15	27.10 ±2.39	35.69 ±4.30	···	0.33±0.05	239 ±24
NGC 1512	0.39 ±0.05	0.24 ±0.03	0.27 ±0.03	0.44 ±0.05	0.43 ±0.02	6.04 ±0.43	22.93 ±2.76	···	···	7.0± 1
NGC 1566	0.75 ±0.10	0.48 ±0.07	0.91 ±0.12	2.11 ±0.26	2.70 ±0.11	31.22 ±2.20	99.95 ±12.00	···	···	400 ±40
NGC 1705	0.026±0.004	0.018±0.003	0.010±0.002	0.017±0.002	0.053±0.002	1.20 ±0.09	1.26 ±0.17	···	···	···
NGC 2403	1.88 ±0.25	1.31 ±0.18	2.13 ±0.27	4.11 ±0.51	5.76 ±0.23	84.00 ±5.88	242.99 ±29.17	···	···	330 ±33
Holmberg II	0.071±0.010	0.057±0.008	0.031±0.005	0.024±0.005	0.17 ±0.01	3.52 ±0.25	4.25 ±0.61	···	···	20 ± 3
M81 Dwarf A	0.002±0.001	0.001±0.001	<0.004	<0.002	<0.018	<0.17	<0.15	···	···	···
DDO 053	0.005±0.001	0.004±0.001	0.003±0.001	0.007±0.001	0.029±0.002	0.34 ±0.03	0.34 ±0.11	···	···	···
NGC 2798	0.11 ±0.02	0.081±0.011	0.27 ±0.03	0.63 ±0.08	2.56 ±0.10	18.24 ±1.49	19.35 ±2.33	···	0.19±0.03	83 ± 9
NGC 2841	1.27 ±0.17	0.75 ±0.10	0.67 ±0.09	1.16 ±0.14	0.90 ±0.04	9.59 ±0.69	57.58 ±6.91	···	···	84 ± 9
NGC 2915	0.054±0.008	0.035±0.005	0.033±0.004	0.031±0.004	0.060±0.003	1.20 ±0.09	1.14 ±0.26	···	···	···
Holmberg I	0.012±0.001	0.008±0.001	0.007±0.002	0.008±0.002	0.013±0.004	0.37 ±0.12	0.90 ±0.20	···	···	···
NGC 2976	0.43 ±0.06	0.28 ±0.04	0.51 ±0.07	1.02 ±0.13	1.36 ±0.05	18.99 ±1.34	49.13 ±5.95	···	0.61±0.24	51 ± 5
NGC 3049	0.040±0.005	0.028±0.004	0.065±0.009	0.14 ±0.02	0.41 ±0.02	2.55 ±0.20	4.25 ±0.52	···	···	12 ± 2
NGC 3031	10.92 ±1.48	6.53 ±0.90	5.96 ±0.75	8.04 ±1.00	5.05 ±0.20	82.54 ±5.78	364.26 ±43.72	···	···	380 ±38
NGC 3034[b]	···	···	···	···	···	···	···	39.2±9.8	5.51±0.83	7660 ±770
Holmberg IX	0.007±0.001	0.004±0.001	<0.013	<0.012	<0.037	<0.25	<0.48	···	···	···
M81 Dwarf B	0.005±0.001	0.004±0.001	0.003±0.001	0.003±0.001	0.008±0.001	0.13 ±0.02	0.22 ±0.15	···	···	···
NGC 3190	0.37 ±0.05	0.24 ±0.03	0.25 ±0.03	0.33 ±0.04	0.27 ±0.01	4.88 ±0.35	13.84 ±1.68	···	0.19±0.04	43 ± 5
NGC 3184	0.56 ±0.08	0.36 ±0.05	0.67 ±0.08	1.44 ±0.18	1.44 ±0.06	15.24 ±1.08	68.42 ±8.22	···	···	56 ± 5
NGC 3198	0.27 ±0.04	0.17 ±0.02	0.34 ±0.04	0.68 ±0.09	1.05 ±0.04	9.64 ±0.68	36.68 ±4.40	···	···	27 ± 3
IC 2574	0.15 ±0.02	0.091±0.013	0.066±0.009	0.066±0.009	0.28 ±0.01	5.10 ±0.37	10.82 ±1.39	···	···	11 ± 2
NGC 3265	0.028±0.004	0.020±0.003	0.041±0.005	0.10 ±0.01	0.29 ±0.01	2.30 ±0.18	2.47 ±0.33	···	···	11 ± 2
Markarian 33	0.027±0.004	0.019±0.003	0.053±0.007	0.13 ±0.02	0.84 ±0.03	3.81 ±0.28	3.63 ±0.46	···	0.04±0.01	17 ± 2
NGC 3351	0.81 ±0.11	0.51 ±0.07	0.73 ±0.09	1.33 ±0.16	2.45 ±0.10	19.26 ±1.42	62.67 ±7.53	···	···	44 ± 5
NGC 3521	2.05 ±0.28	1.36 ±0.19	2.56 ±0.32	6.27 ±0.76	5.47 ±0.22	57.24 ±4.08	216.85 ±26.06	···	2.11±0.82	357 ±36

Note. — See § 3 for details on the data. Upper limits (3σ) are provided for non-detections.

[a]Possibly severely contaminated by background source(s).

[b]The bright core of NGC 3034 (M 82) has rendered the *Spitzer* data extremely difficult to process. Saturation effects severely limit our ability to extract reliable global flux densities.

Table 3. Infrared, Submillimeter, and Radio Flux Densities (continued)

Galaxy	3.6 μm (Jy)	4.5 μm (Jy)	5.8 μm (Jy)	8.0 μm (Jy)	24 μm (Jy)	70 μm (Jy)	160 μm (Jy)	450 μm (Jy)	850 μm (Jy)	20 cm (Jy)
NGC 3621	0.99 ±0.13	0.67 ±0.09	1.62 ±0.21	3.51 ±0.44	3.38 ±0.14	45.25 ±3.18	132.39 ±15.90	···	···	198 ±20
NGC 3627	1.87 ±0.25	1.25 ±0.17	2.39 ±0.30	5.58 ±0.69	7.39 ±0.30	82.14 ±6.16	218.40 ±26.21	···	1.86±0.70	458 ±46
NGC 3773	0.022±0.003	0.014±0.002	0.026±0.004	0.048±0.006	0.14 ±0.01	1.35 ±0.12	2.23 ±0.35	···	···	5.8±0.5
NGC 3938	0.32 ±0.04	0.21 ±0.03	0.41 ±0.05	0.98 ±0.12	1.07 ±0.04	13.44 ±0.95	49.09 ±5.90	···	···	62 ± 7
NGC 4125	0.64 ±0.09	0.37 ±0.05	0.25 ±0.03	0.14 ±0.02	0.070±0.003	0.95 ±0.09	1.39 ±0.22	···	···	<50
NGC 4236	0.25 ±0.03	0.21 ±0.03	0.11 ±0.01	0.22 ±0.03	0.54 ±0.02	7.84 ±0.56	19.80 ±2.51	···	···	28 ± 3
NGC 4254	0.70 ±0.10	0.47 ±0.06	1.49 ±0.19	3.94 ±0.49	4.17 ±0.17	44.57 ±3.16	138.29 ±16.60	···	1.01±0.54	422 ±42
NGC 4321	0.95 ±0.13	0.64 ±0.09	1.22 ±0.15	2.89 ±0.36	3.39 ±0.14	36.65 ±2.59	134.74 ±16.17	···	0.88±0.49	340 ±34
NGC 4450	0.53 ±0.07	0.33 ±0.04	0.26 ±0.03	0.27 ±0.03	0.20 ±0.01	2.72 ±0.21	14.41 ±1.74	···	···	9.4± 1
NGC 4536	0.40 ±0.05	0.29 ±0.04	0.62 ±0.08	1.66 ±0.21	3.44 ±0.14	27.19 ±2.10	57.07 ±6.86	···	0.42±0.11	194 ±19
NGC 4552	0.83 ±0.11	0.49 ±0.07	0.32 ±0.04	0.17 ±0.02	0.063±0.003	0.11 ±0.03	0.43 ±0.42	···	···	100 ± 3
NGC 4559	0.35 ±0.05	0.23 ±0.03	0.42 ±0.05	0.84 ±0.10	1.10 ±0.04	15.86 ±1.12	49.12 ±5.91	···	···	65 ± 7
NGC 4569	0.76 ±0.10	0.47 ±0.06	0.59 ±0.08	1.02 ±0.13	1.44 ±0.06	10.86 ±0.78	40.09 ±4.84	···	0.47±0.08	83 ± 9
NGC 4579	0.87 ±0.12	0.52 ±0.07	0.54 ±0.07	0.73 ±0.09	0.75 ±0.03	9.12 ±0.66	40.99 ±4.94	···	0.44±0.07	98 ±10
NGC 4594	3.94 ±0.53	2.31 ±0.32	1.75 ±0.22	1.30 ±0.16	0.67 ±0.03	7.43 ±0.56	38.65 ±4.67	···	0.37±0.11	137 ±14
NGC 4625	0.049±0.006	0.030±0.004	0.059±0.008	0.13 ±0.02	0.13 ±0.01	1.89 ±0.14	4.94 ±0.60	···	···	7.1± 2
NGC 4631	1.26 ±0.17	0.84 ±0.11	2.49 ±0.31	5.86 ±0.73	8.12 ±0.33	118.67 ±9.02	282.27 ±33.88	30.7±10.0	5.73±1.21	1200 ±120
NGC 4725	1.14 ±0.15	0.70 ±0.10	0.75 ±0.10	1.21 ±0.15	0.83 ±0.03	8.28 ±0.56	56.05 ±6.76	···	···	28 ± 3
NGC 4736	3.60 ±0.49	2.32 ±0.32	2.76 ±0.35	5.17 ±0.64	5.61 ±0.23	85.08 ±6.66	178.68 ±21.45	···	1.54±0.66	271 ±27
DDO 154	0.004±0.001	0.003±0.001	<0.006	<0.004	0.006±0.002[a]	0.048±0.03[a]	0.27 ±0.14[a]	···	···	···
NGC 4826	2.52 ±0.34	1.57 ±0.22	1.66 ±0.21	2.35 ±0.29	2.52 ±0.10	44.42 ±3.67	89.60 ±10.78	···	1.23±0.31	101 ±10
DDO 165	0.016±0.002	0.012±0.002	0.005±0.002	0.004±0.001[a]	0.013±0.002[a]	0.14 ±0.05[a]	0.34 ±0.15[a]	···	···	···
NGC 5033	0.64 ±0.09	0.47 ±0.06	0.82 ±0.10	1.92 ±0.24	1.96 ±0.08	24.90 ±1.80	92.50 ±11.11	···	1.10±0.55	178 ±18
NGC 5055	2.38 ±0.32	1.55 ±0.21	2.67 ±0.34	5.64 ±0.70	5.70 ±0.23	68.41 ±4.86	300.46 ±36.06	···	···	390 ±39
NGC 5194	2.66 ±0.36	1.80 ±0.25	4.29 ±0.54	10.64 ±1.32	12.50 ±0.50	145.49 ±10.29	518.73 ±62.46	···	2.61±0.39	1490 ±150
NGC 5195	0.83 ±0.11	0.51 ±0.07	0.47 ±0.06	0.65 ±0.08	1.34 ±0.05	13.09 ±1.01	12.94 ±1.59	···	0.26±0.04	50 ± 5
Tololo 89	0.038±0.005	0.025±0.004	0.014±0.002	0.059±0.008	0.26 ±0.01	1.69 ±0.13	2.83 ±0.42	···	···	4.2±0.8
NGC 5408	0.052±0.007	0.037±0.005	0.041±0.005	0.038±0.005	0.43 ±0.02	3.27 ±0.24	2.32 ±0.36	···	···	···
NGC 5474	0.10 ±0.01	0.073±0.010	0.077±0.010	0.12 ±0.01	0.18 ±0.01	3.51 ±0.28	9.96 ±1.22	···	···	12 ± 2
NGC 5713	0.20 ±0.03	0.14 ±0.02	0.30 ±0.04	1.16 ±0.15	2.32 ±0.09	20.79 ±1.60	36.48 ±4.38	···	0.57±0.12	160 ±16
NGC 5866	0.66 ±0.09	0.42 ±0.06	0.31 ±0.04	0.31 ±0.04	0.20 ±0.01	7.69 ±0.55	17.34 ±2.09	0.8±0.2	0.14±0.02	23 ± 3
IC 4710	0.070±0.010	0.047±0.007	0.045±0.006	0.065±0.008	0.11 ±0.01	2.18 ±0.18	3.31 ±0.46	···	···	···
NGC 6822	2.12 ±0.29	1.38 ±0.19	1.45 ±0.18	1.41 ±0.18	2.59 ±0.10	59.23 ±4.17	142.98 ±17.20	···	···	69 ±14
NGC 6946	3.31 ±0.45	2.18 ±0.30	5.88 ±0.74	14.12 ±1.76	21.66 ±0.87	206.74 ±16.08	523.16 ±62.86	18.5±4.6	2.98±0.45	1395 ±140
NGC 7331	1.61 ±0.22	1.02 ±0.14	1.87 ±0.24	4.05 ±0.50	4.01 ±0.16	66.06 ±4.80	172.24 ±20.67	20.6±8.1	2.11±0.38	373 ±37
NGC 7552	0.45 ±0.06	0.36 ±0.05	1.07 ±0.14	2.71 ±0.34	10.50 ±0.42[b]	58.20 ±9.53[b]	90.92 ±10.92	···	0.80±0.17	276 ±28
NGC 7793	0.77 ±0.10	0.47 ±0.06	1.04 ±0.13	1.85 ±0.23	2.01 ±0.08	33.06 ±2.32	125.43 ±15.07	···	···	103 ±10

Note. — See § 3 for details on the data. Upper limits (3σ) are provided for non-detections.

[a]Possibly severely contaminated by background sources(s).

[b]Flux artificially low due to saturation effects.

Table 4. IRAC Aperture Correction Parameters

λ	A	B	C
3.5 μm	0.82	0.370	0.910
4.5 μm	1.00	0.380	0.940
5.8 μm	1.49	0.207	0.720
8.0 μm	1.37	0.330	0.740

Note. — See § 3 and spider.ipac.caltech.edu/staff/jarrett/irac/calibration/

Table 5. Infrared and Submillimeter Aperture Correction Factors

Galaxy	24 μm	70 μm	160 μm	450 μm	850 μm
NGC 0024	1.06	1.10	1.20	···	···
NGC 0337	1.01	1.06	1.15	···	···
NGC 0584	1.00	1.04	1.11	···	···
NGC 0628	1.02	1.03	1.06	···	···
NGC 0855	1.02	1.07	1.15	···	···
NGC 0925	1.03	1.04	1.07	···	···
NGC 1097	1.01	1.02	1.06	···	2.09
NGC 1266	1.01	1.05	1.13	···	···
NGC 1291	1.01	1.02	1.04	···	···
NGC 1316	1.06	1.02	1.18	···	···
NGC 1377	1.02	1.06	1.15	···	···
NGC 1404	1.00	1.02	1.07	···	···
NGC 1482	1.00	1.03	1.10	···	···
NGC 1512	1.04	1.05	1.06	···	···
NGC 1566	1.04	1.05	1.04	···	···
NGC 1705	1.04	1.12	1.19	···	···
NGC 2403	1.00	1.00	1.02	···	···
Holmberg II	1.00	1.02	1.09	···	···
M81 Dwarf A	1.00	1.00	1.00	···	···
DDO 053	1.03	1.15	1.48	···	···
NGC 2798	1.03	1.08	1.19	···	1.08
NGC 2841	1.01	1.04	1.10	···	···
NGC 2915	1.07	1.15	1.33	···	···
Holmberg I	1.01	1.05	1.15	···	···
NGC 2976	1.00	1.03	1.10	···	1.56
NGC 3049	1.02	1.07	1.18	···	···
NGC 3031	1.00	1.00	1.01	···	···
NGC 3034	1.00	1.00	1.00	···	···
Holmberg IX	1.00	1.00	1.00	···	···
M81 Dwarf B	1.12	1.16	1.86	···	···
NGC 3190	1.01	1.05	1.13	···	1.12
NGC 3184	1.00	1.00	1.05	···	···
NGC 3198	1.00	1.02	1.08	···	···
IC 2574	1.04	1.07	1.12	···	···
NGC 3265	1.02	1.07	1.16	···	···
Markarian 33	1.02	1.07	1.16	···	···
NGC 3351	1.04	1.06	1.11	···	···
NGC 3521	1.00	1.01	1.05	···	1.56

Note. — IRAC aperture corrections are described by Equation 1. See § 3.4 and Dale et al. (2005) for details.

Table 4. Infrared and Submillimeter Aperture Correction Factors (continued)

Galaxy	24 μm	70 μm	160 μm	450 μm	850 μm
NGC 3621	1.07	1.09	1.12	···	···
NGC 3627	1.00	1.01	1.06	···	1.53
NGC 3773	1.07	1.13	1.15	···	···
NGC 3938	1.01	1.03	1.08	···	···
NGC 4125	1.09	1.16	1.31	···	···
NGC 4236	1.00	1.02	1.06	···	···
NGC 4254	1.00	1.02	1.07	···	2.06
NGC 4321	1.00	1.01	1.06	···	2.19
NGC 4450	1.08	1.12	1.21	···	···
NGC 4536	1.00	1.02	1.08	···	1.30
NGC 4552	1.03	1.10	1.28	···	···
NGC 4559	1.00	1.03	1.09	···	···
NGC 4569	1.00	1.01	1.07	···	1.11
NGC 4579	1.01	1.04	1.12	···	···
NGC 4594	1.09	1.12	1.21	···	1.33
NGC 4625	1.01	1.06	1.16	···	···
NGC 4631	1.00	1.00	1.05	1.27	1.17
NGC 4725	1.03	1.05	1.10	···	···
NGC 4736	1.00	1.00	1.02	···	1.67
DDO 154	1.06	1.14	1.35	···	···
NGC 4826	1.08	1.09	1.14	···	1.24
DDO 165	1.02	1.09	1.24	···	···
NGC 5033	1.00	1.01	1.05	···	1.93
NGC 5055	1.00	1.00	1.03	···	···
NGC 5194	1.00	1.00	1.01	···	···
NGC 5195	1.01	1.06	1.13	···	···
Tololo 89	1.08	1.17	1.38	···	···
NGC 5408	1.01	1.05	1.12	···	···
NGC 5474	1.00	1.03	1.09	···	···
NGC 5713	1.01	1.06	1.14	···	1.17
NGC 5866	1.00	1.03	1.09	···	···
IC 4710	1.03	1.08	1.19	···	···
NGC 6822	1.00	1.00	1.01	···	···
NGC 6946	1.00	1.00	1.03	···	···
NGC 7331	1.08	1.10	1.16	1.44	1.11
NGC 7552	1.01	1.02	1.13	···	1.17
NGC 7793	1.01	1.03	1.08	···	···

Note. — IRAC aperture corrections are described by Equation 1. See § 3.4 and Dale et al. (2005) for details.

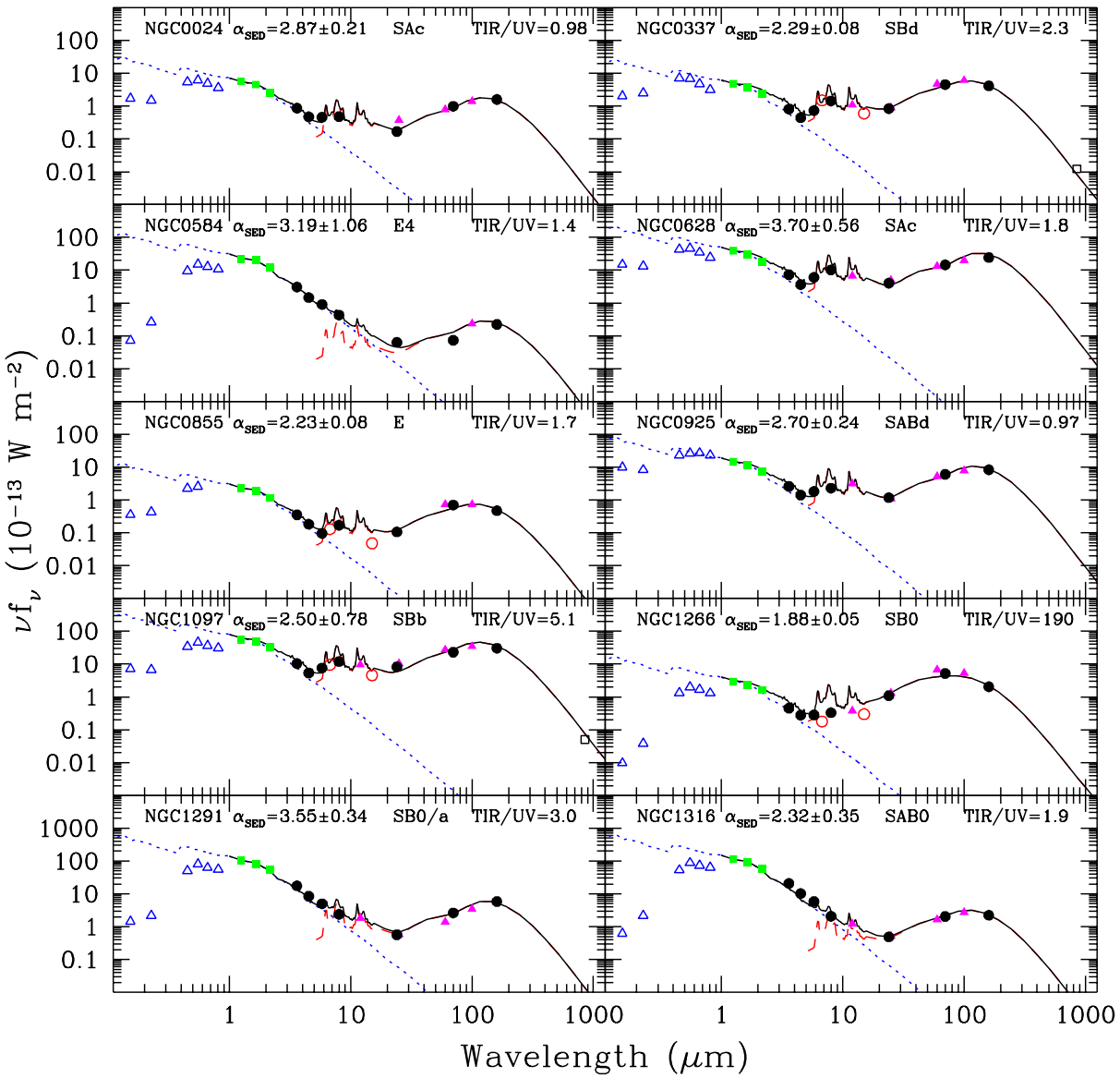

Fig. 1.— Globally-integrated 0.15-850 μm spectral energy distributions for the SINGS sample. *GALEX* and optical, 2MASS, *Spitzer*, *IRAS*, *ISO*, and SCUBA data are represented by open triangles, filled squares, filled circles, filled triangles, open circles, and open squares, respectively. The solid curve is the sum of a dust (dashed) and a stellar (dotted) model. The dust curve is a Dale & Helou (2002) model fitted to ratios of the 24, 70, and 160 μm fluxes; the $\alpha_{\rm SED}$ listed within each panel parametrizes the distribution of dust mass as a function of heating intensity, as described in Dale & Helou (2002). The stellar curve is a 1 Gyr continuous star formation, solar metallicity curve from Vazquez & Leitherer (2005) fitted to the 2MASS data (see § 4 for details).

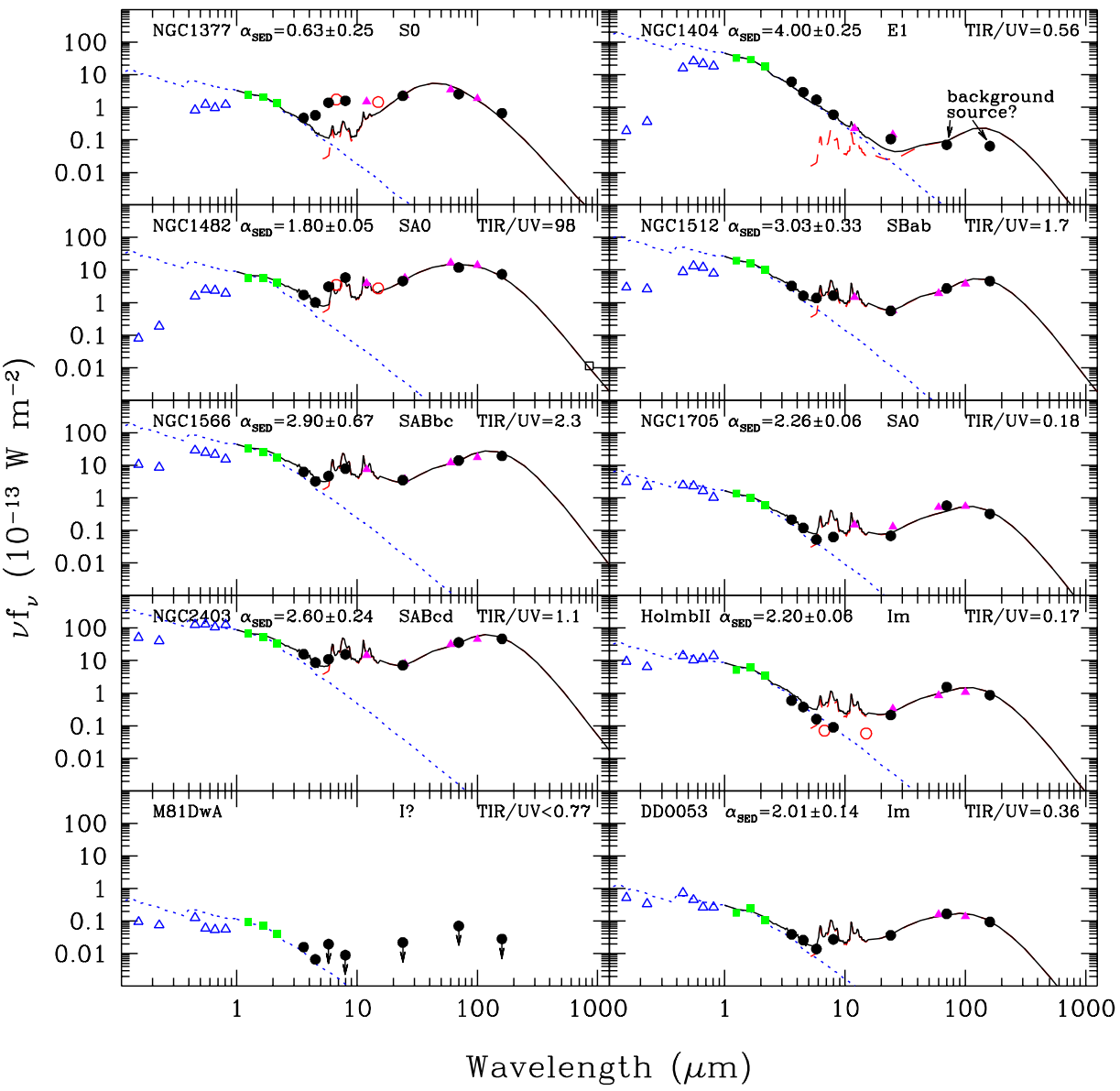

Fig. 2.— Globally-integrated 0.15-850 μm spectral energy distributions for the SINGS sample (continued).

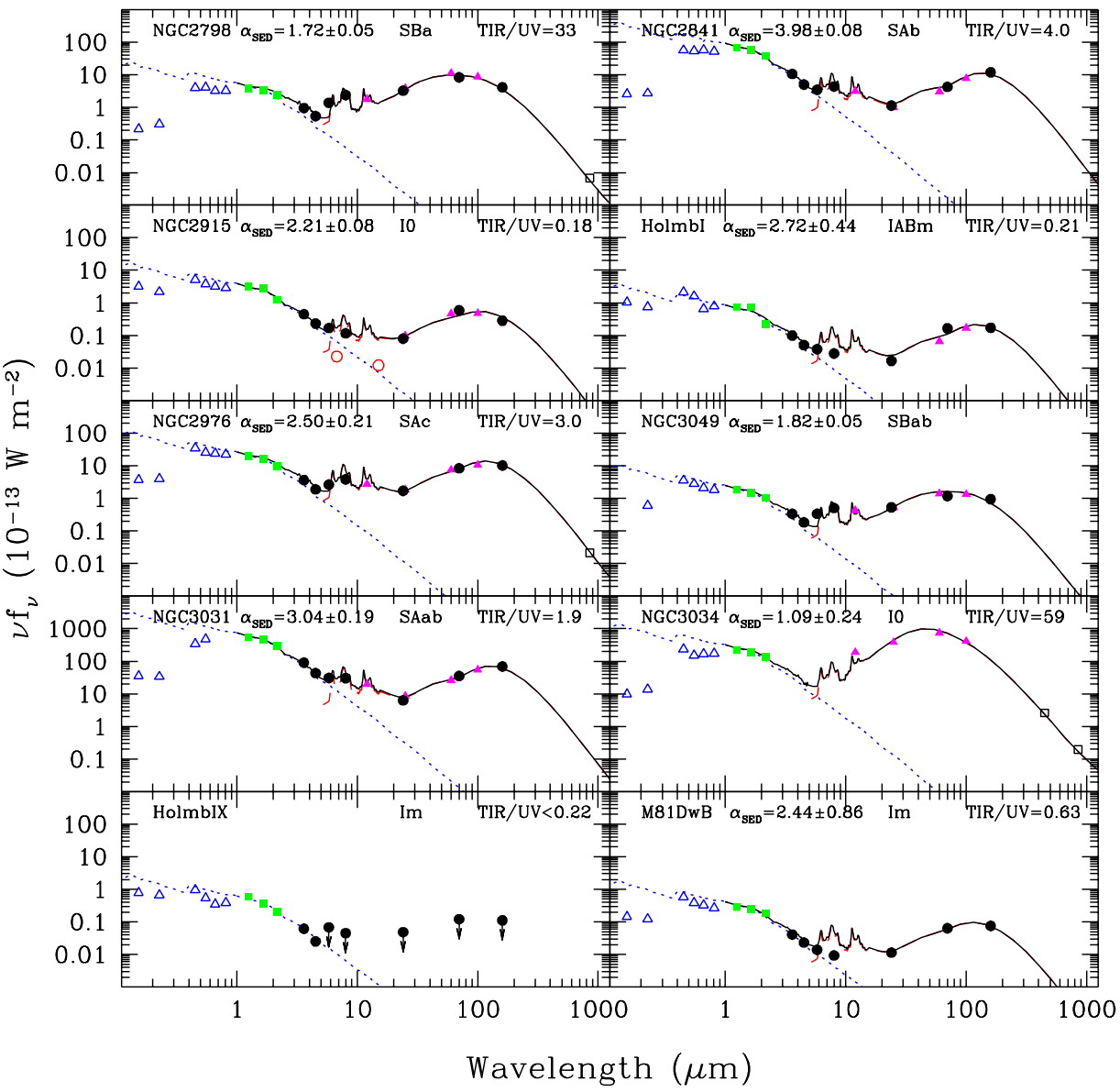

Fig. 3.— Globally-integrated 0.15-850 μm spectral energy distributions for the SINGS sample (continued).

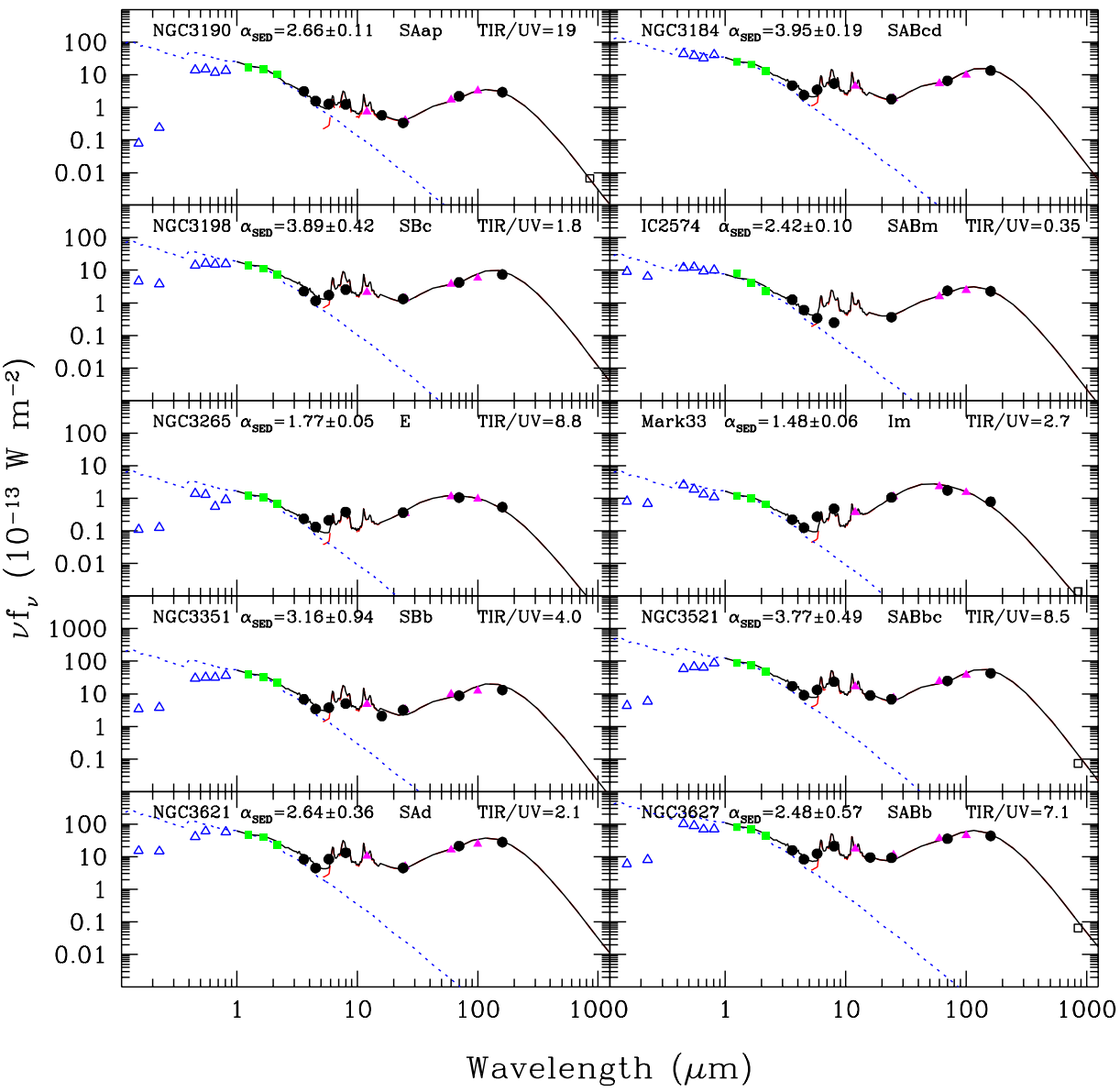

Fig. 4.— Globally-integrated 0.15-850 μm spectral energy distributions for the SINGS sample (continued).

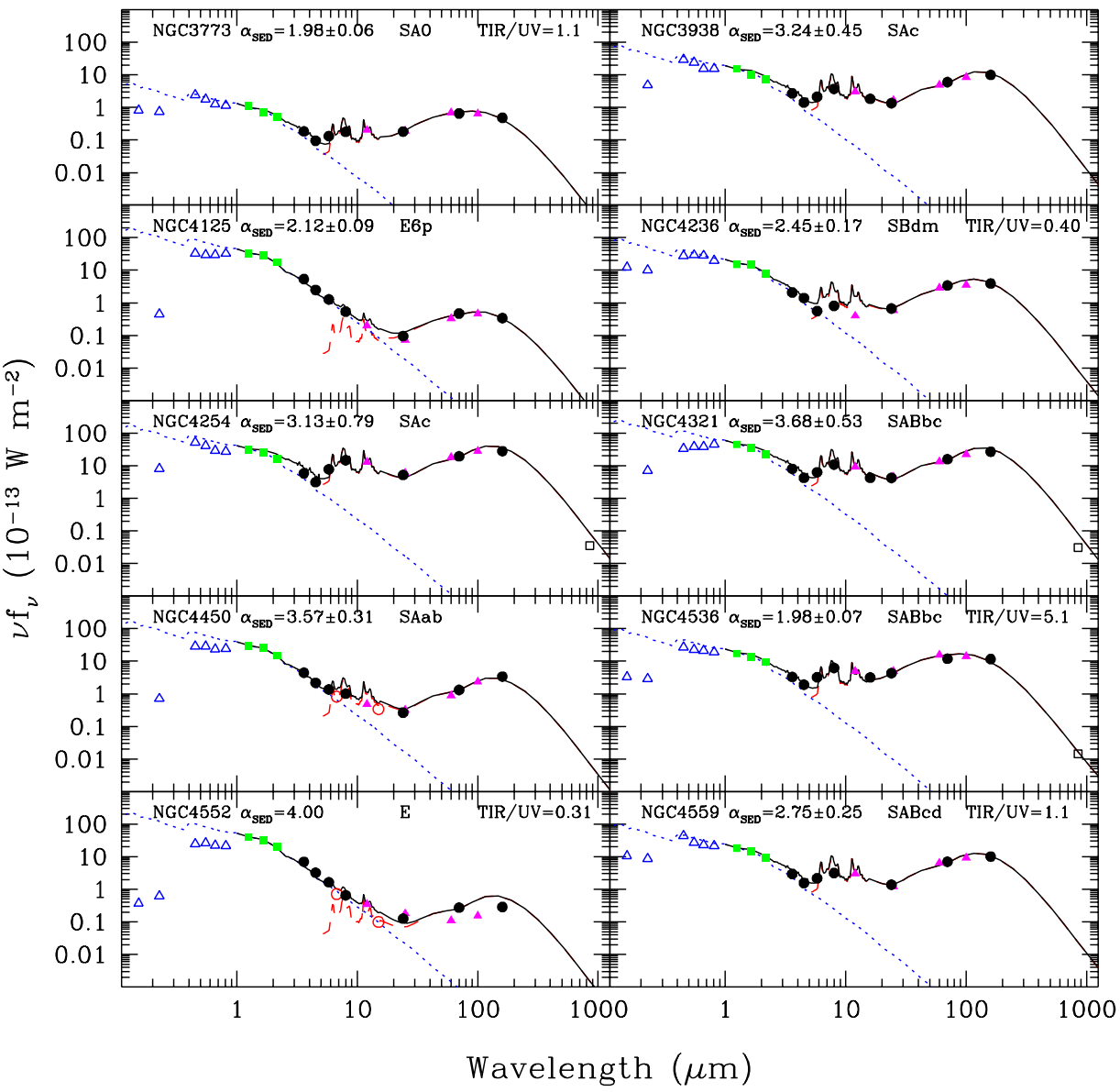

Fig. 5.— Globally-integrated 0.15-850 μm spectral energy distributions for the SINGS sample (continued).

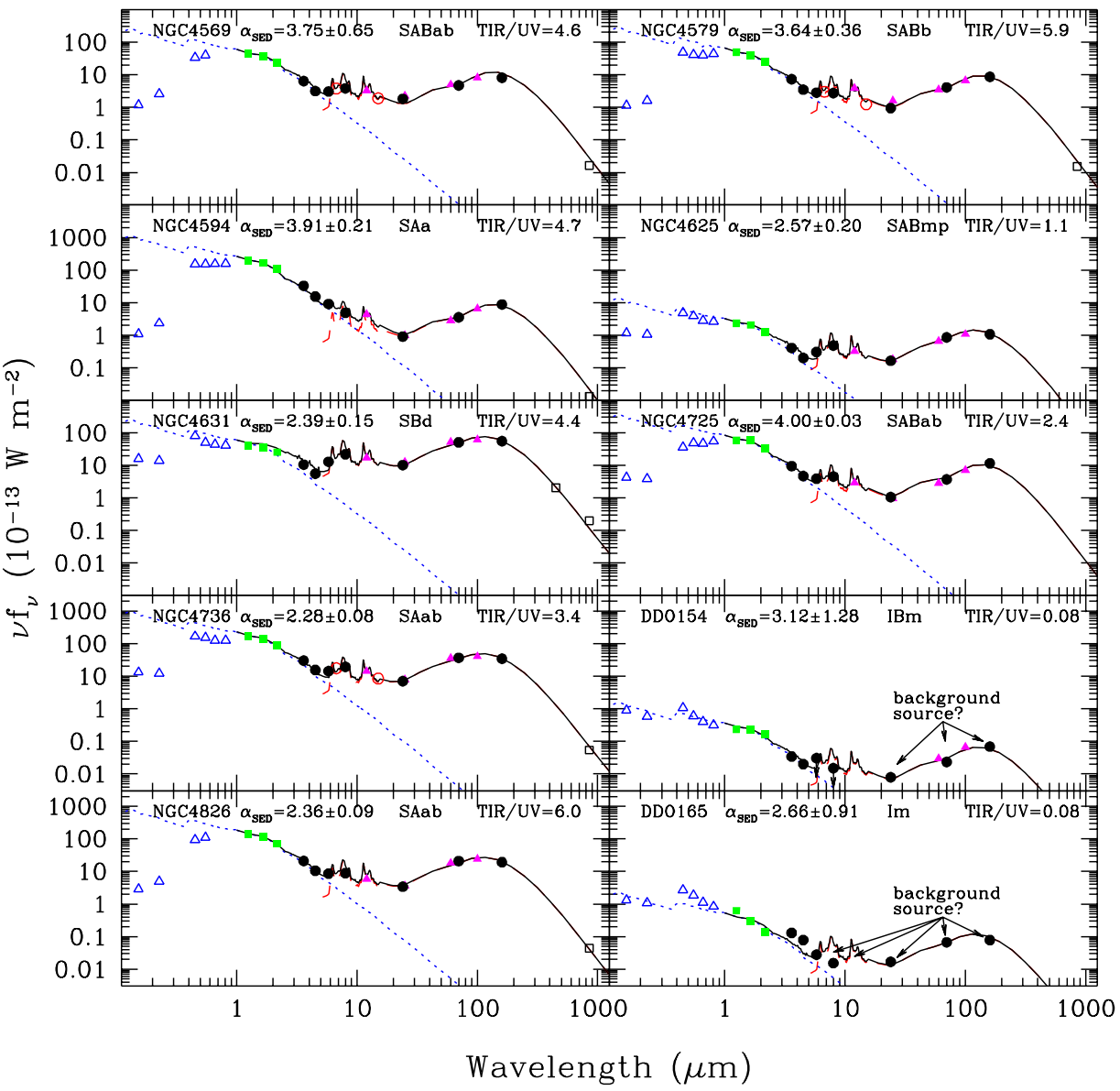

Fig. 6.— Globally-integrated 0.15-850 μm spectral energy distributions for the SINGS sample (continued).

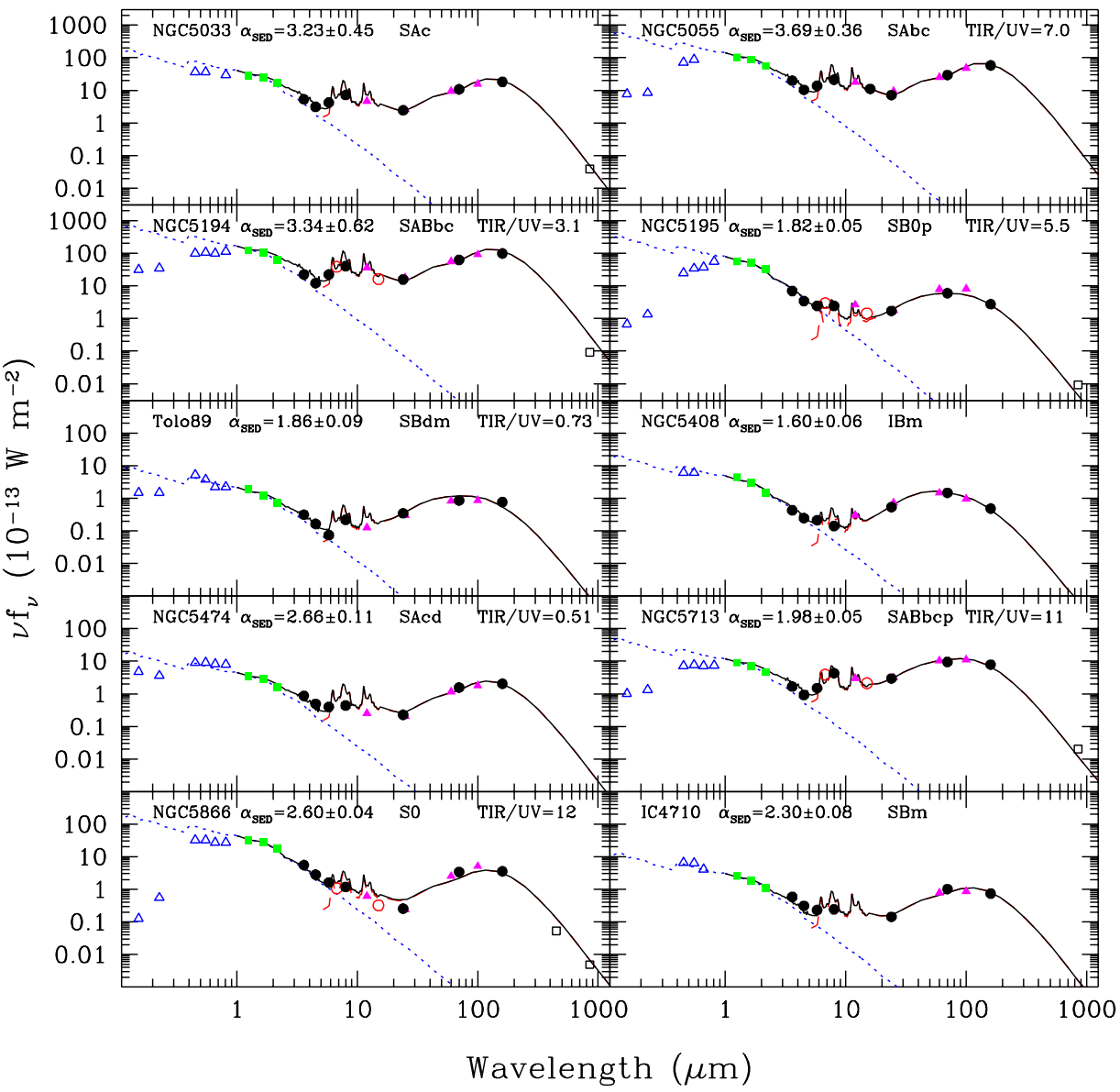

Fig. 7.— Globally-integrated 0.15-850 μm spectral energy distributions for the SINGS sample (continued).

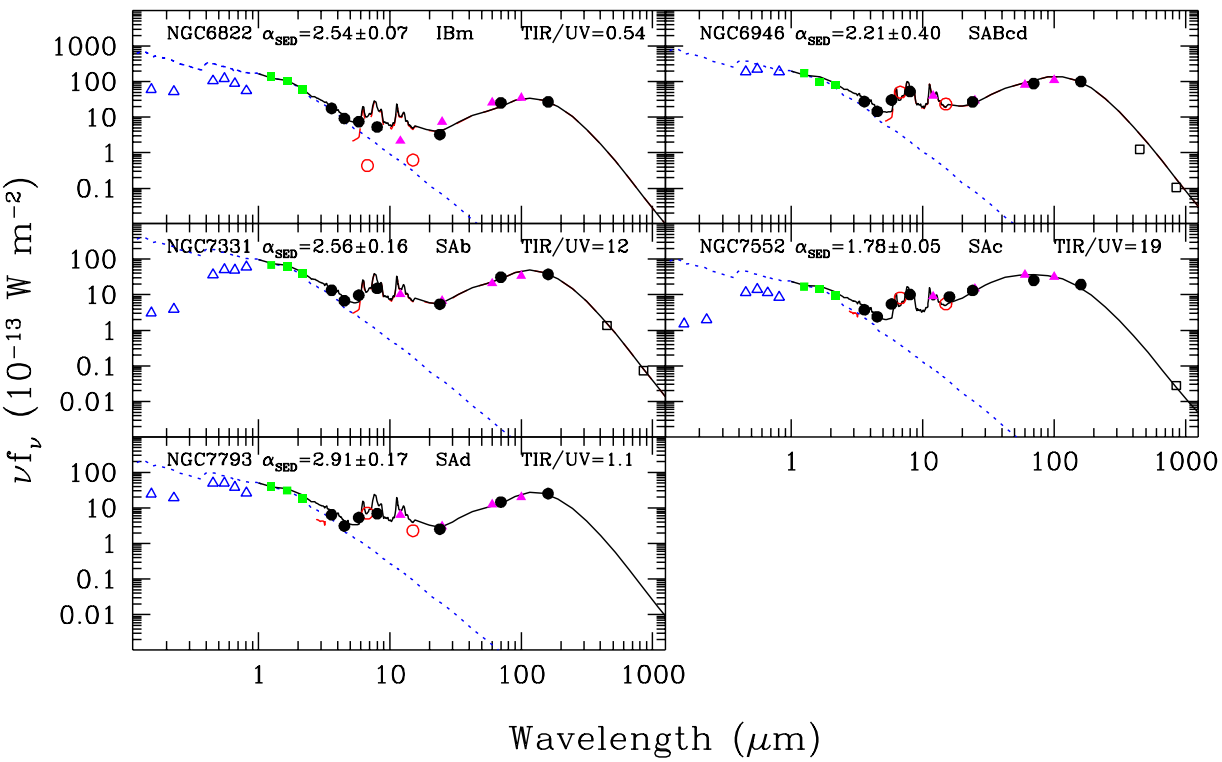

Fig. 8.— Globally-integrated 0.15-850 μm spectral energy distributions for the SINGS sample (continued).

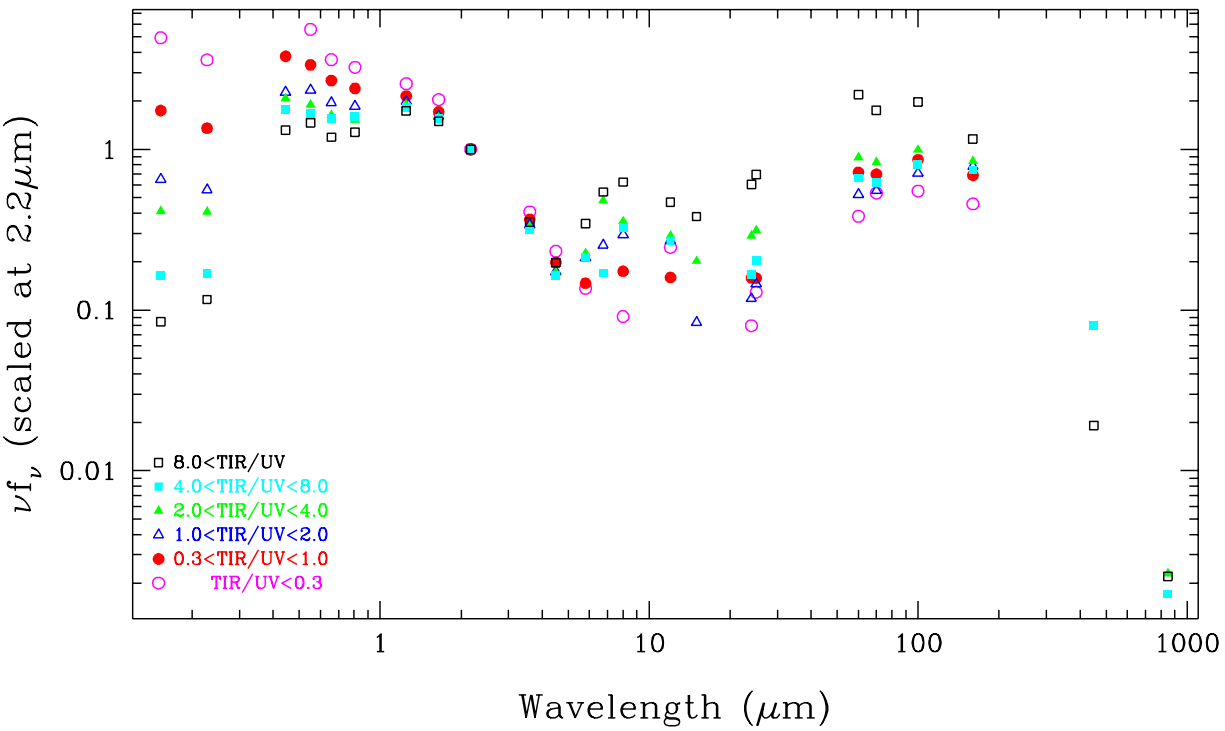

Fig. 9.— A display of stacked spectral energy distributions that emphasizes the infrared-to-ultraviolet variations within the SINGS sample. Each spectral energy distribution in the stack represents an average of approximately 10 individual spectral energy distributions that fall within a given bin of the infrared-to-ultraviolet ratio.

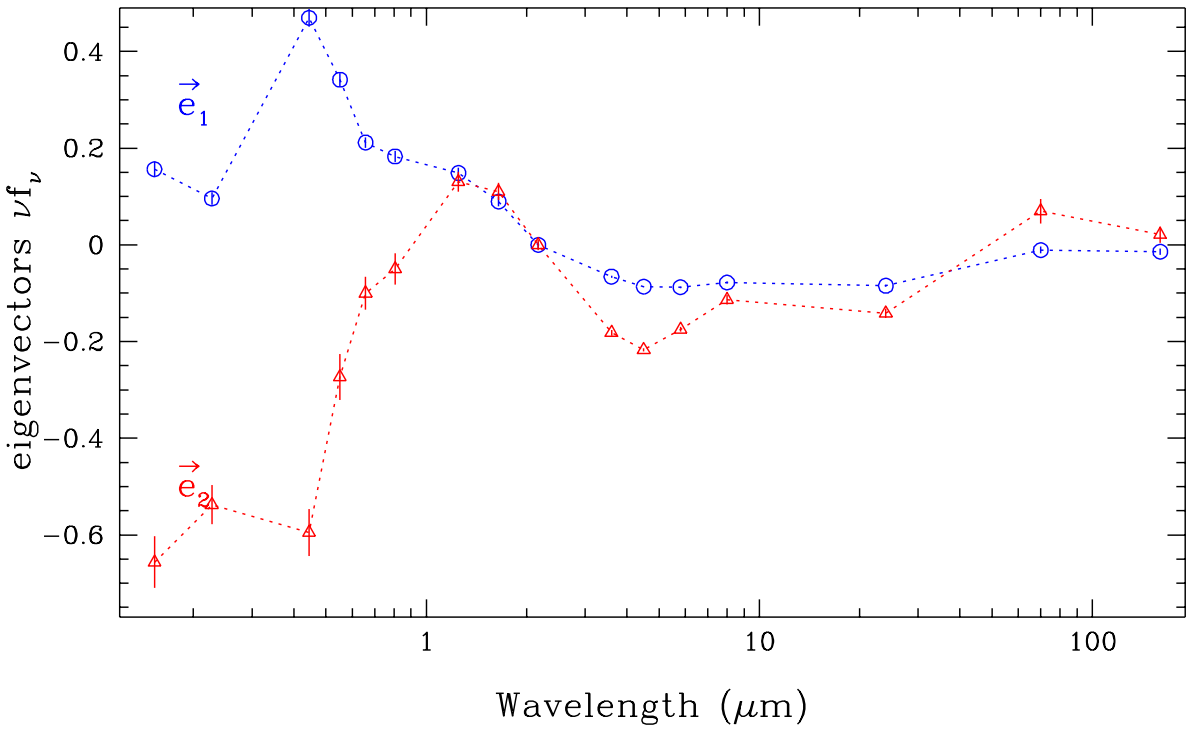

Fig. 10.— The strongest (circles) and second strongest (triangles) eigenvector spectra from a principal component analysis of the SINGS spectra are displayed. These are average eigenvectors stemming from 10,000 Monte Carlo simulations based on the observed fluxes and their uncertainties (corrected for Galactic extinction and airmass in the case of ground-based observations); the error bars shown in this figure indicate the dispersion of the eigenspectra from the simulations. These eigenvectors have normalized eigenvalues of 0.84 and 0.10; $\langle\vec{e}_1\rangle$ and $\langle\vec{e}_2\rangle$ respectively contribute to 84% and 10% of the observed variation in the sample spectra.

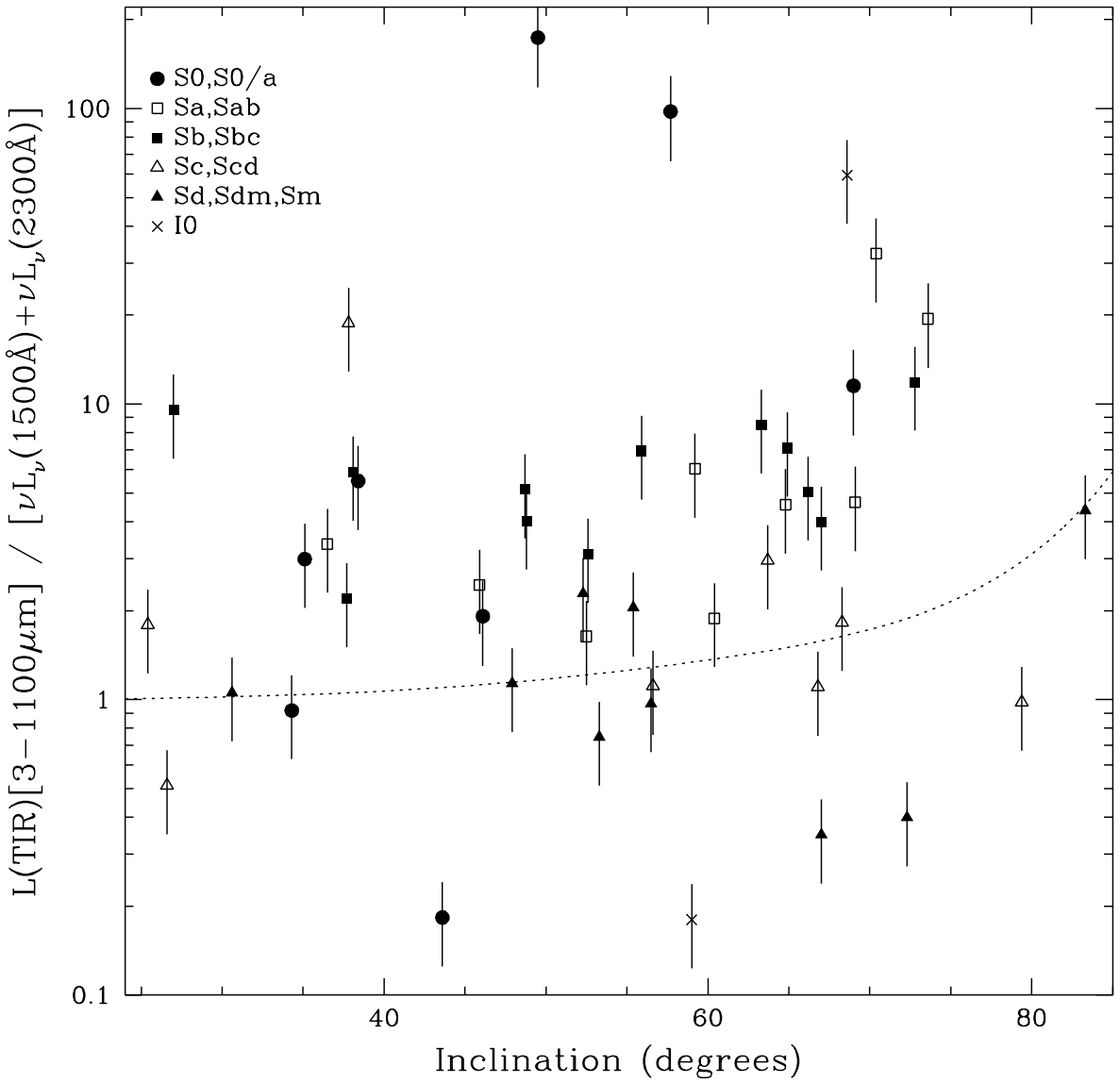

Fig. 11.— The infrared-to-ultraviolet ratio as a function of galaxy disk inclination. The (arbitrarily normalized) dotted line shows the expected effect of extinction on the ultraviolet data with changing inclination using the thin disk model and a central face-on optical depth in the B band of $\tau_B^{\rm f} = 2$ described in Tuffs et al. (2004). The error bars stem from the observational uncertainties.

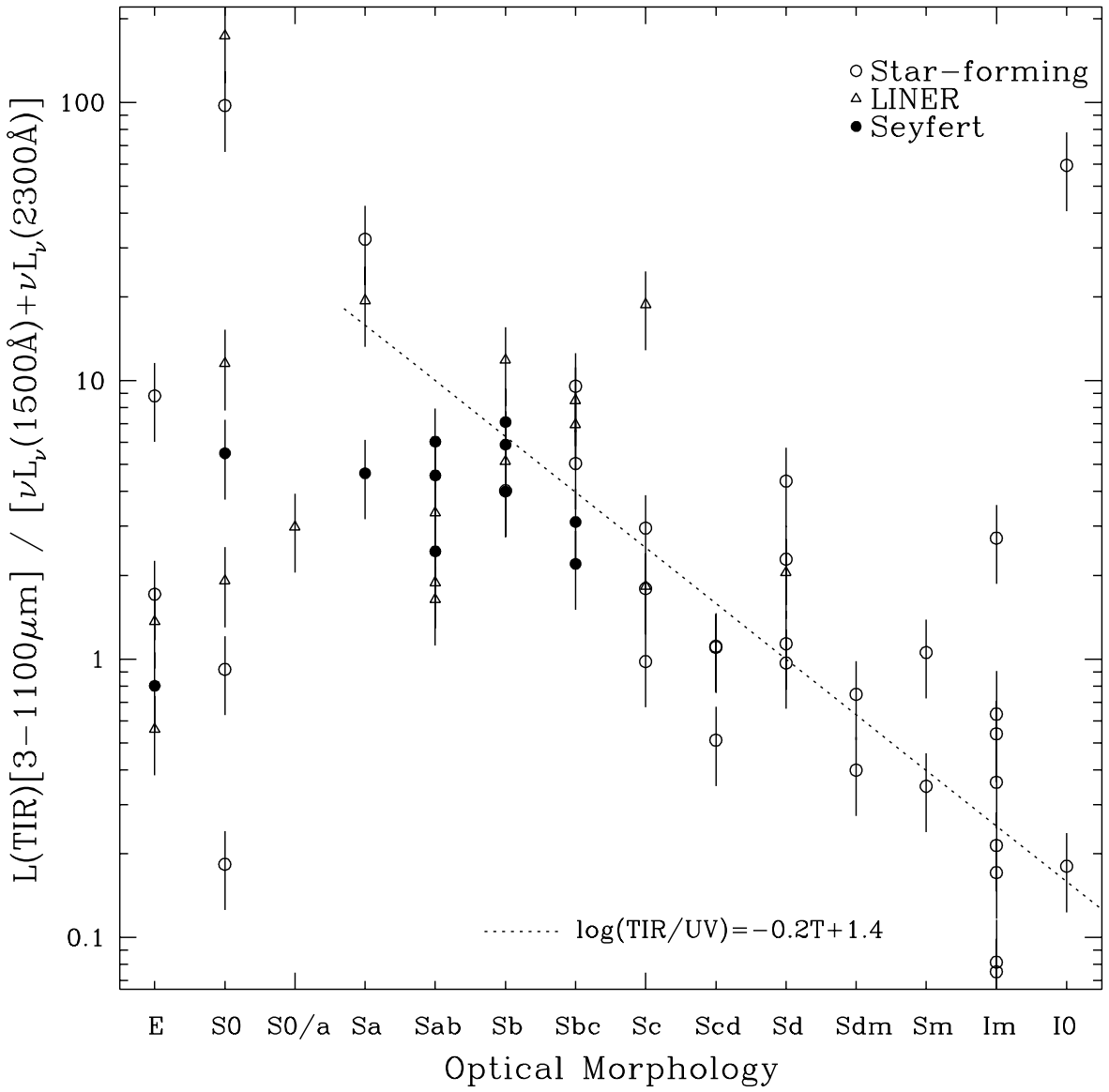

Fig. 12.— The infrared-to-ultraviolet ratio as a function of galaxy optical morphology. The equation provided quantifies the approximate trend with Hubble type for late-type galaxies shown as a dotted curve (e.g., Sa→ T =1, Sb→ T =3, Sc→ T =5, etc.).

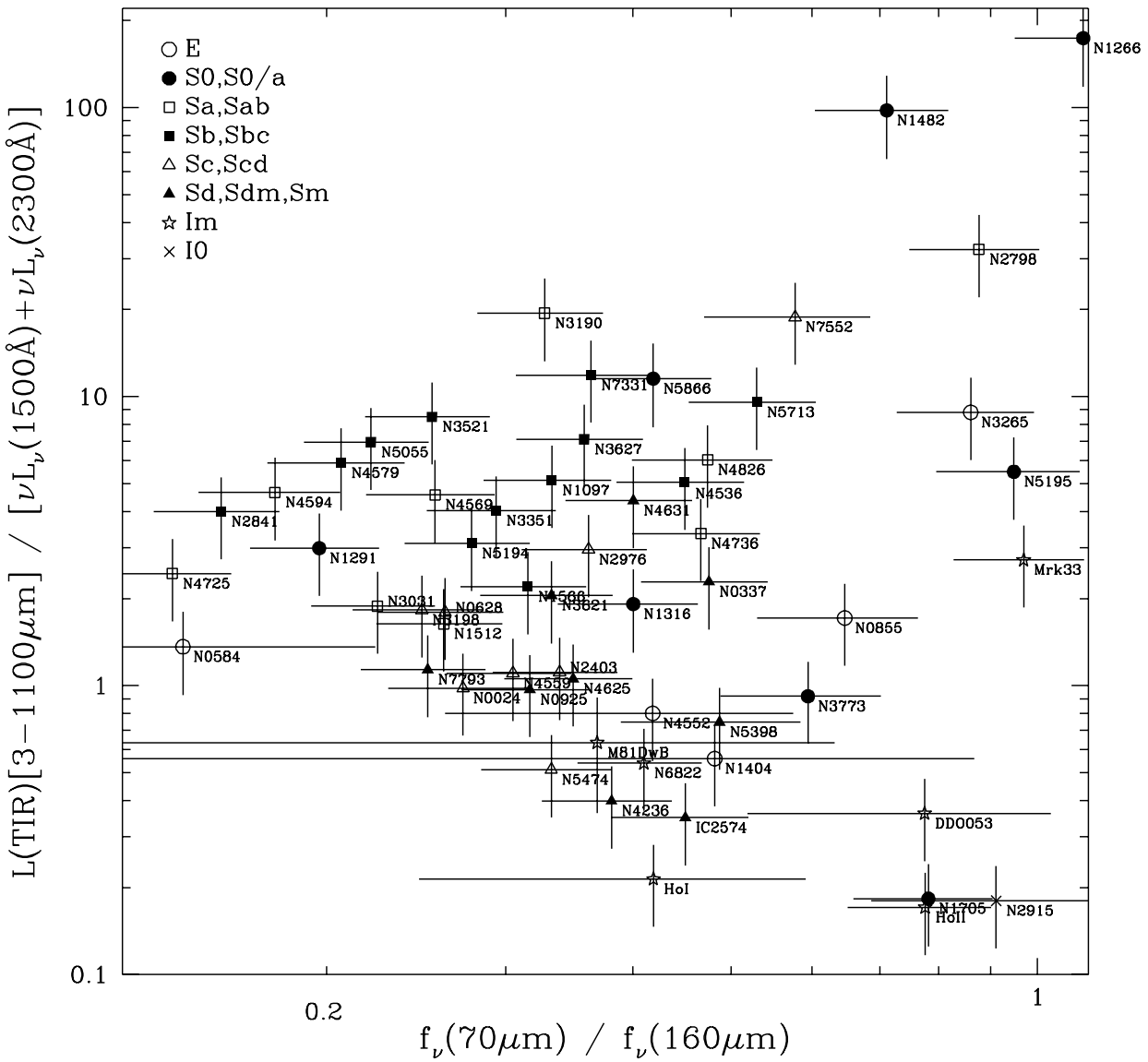

Fig. 13.— The infrared-to-ultraviolet ratio as a function of far-infrared color.

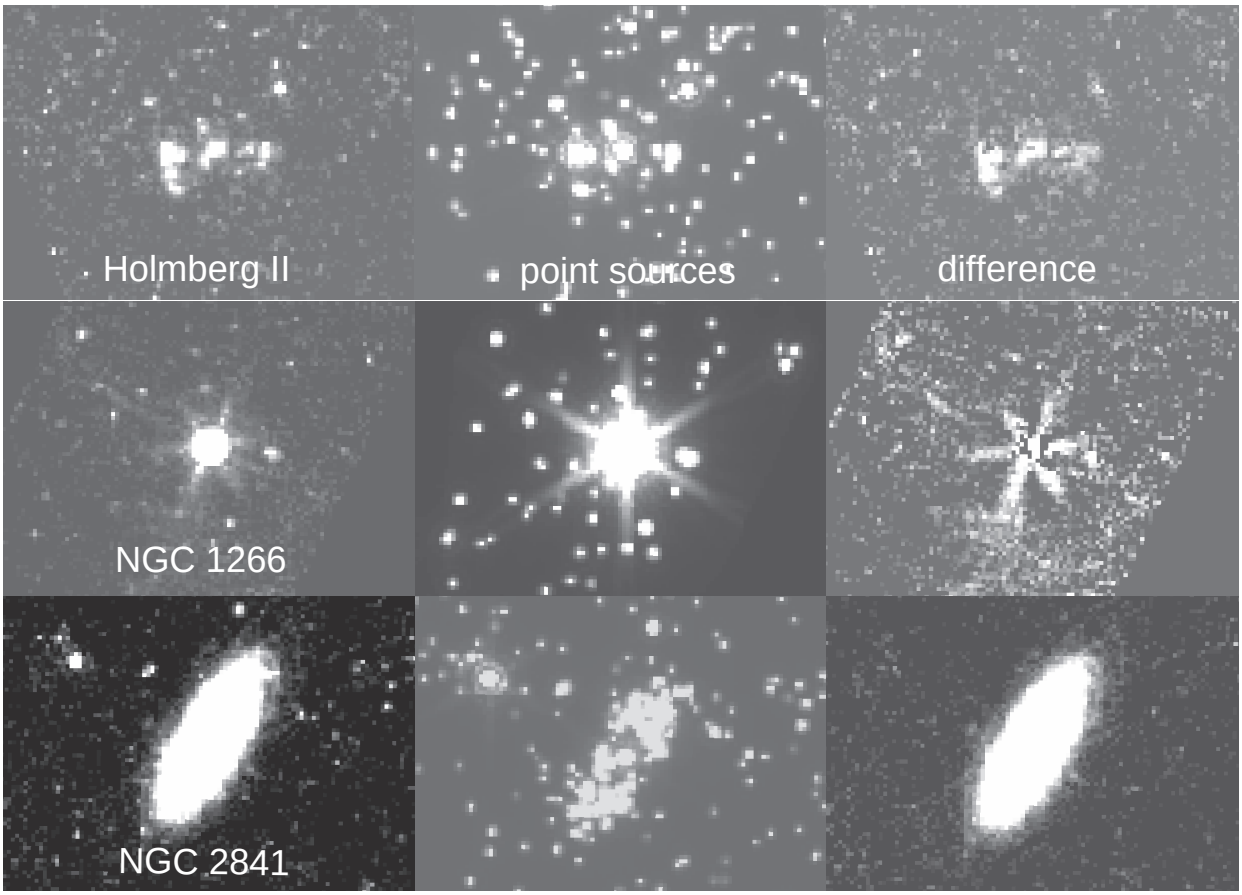

Fig. 14.— Examples of galaxies with clumpy (Holmberg II), unresolved (NGC 1266), and smooth (NGC 2841) 24 μm emission. The left, middle, and right panels respectively show the original 24 μm images, images of the point sources therein, and the differences in the original and point source images (see § 5.3).

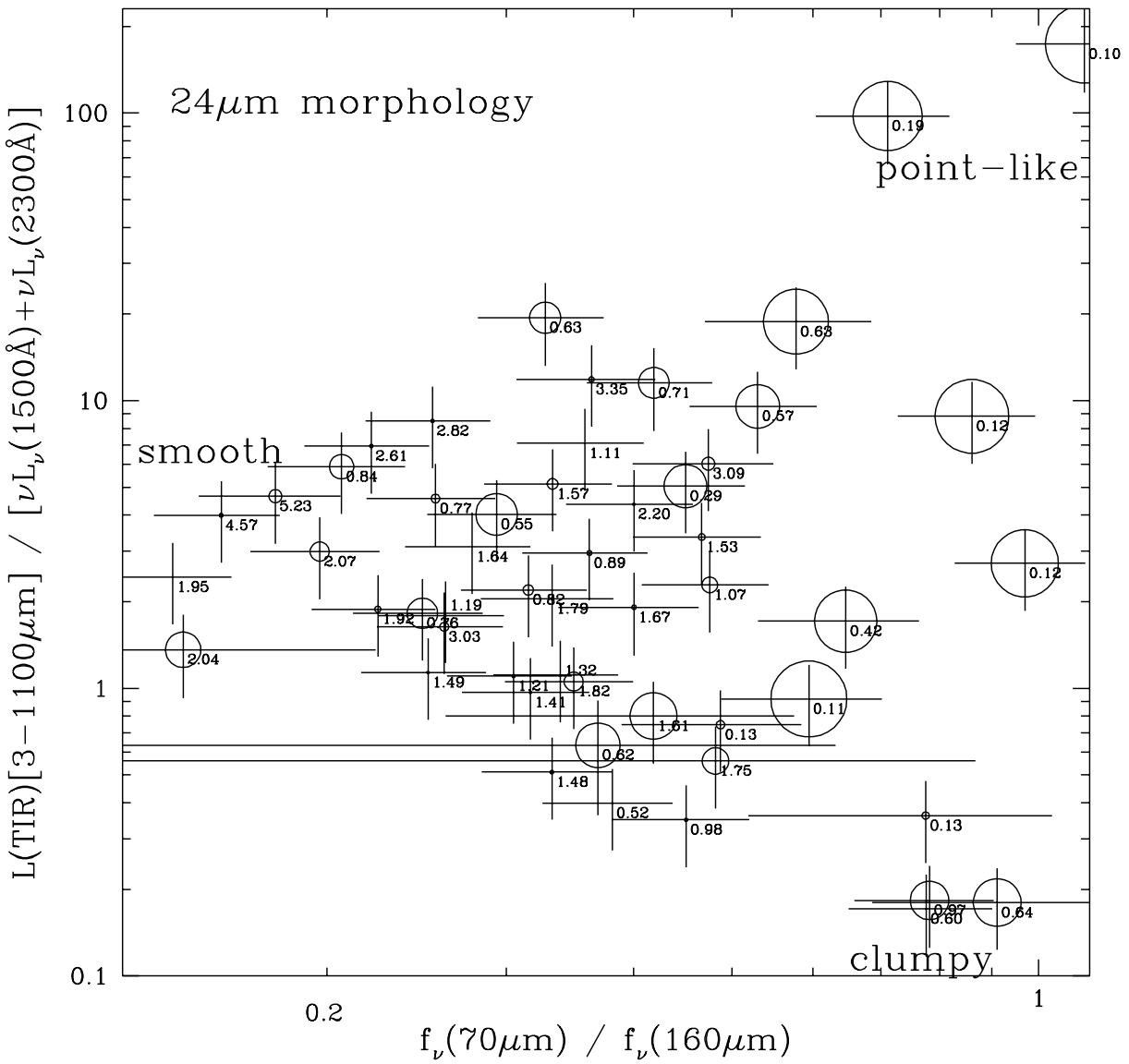

Fig. 15.— Similar to Figure 13, but with symbol size scaled according to the ratio of nuclear-to-total 24 μm emission; the largest symbols have this ratio equal to $\sim$0.9. Listed near each data point is the ratio of resolved-to-unresolved 24 μm emission (see Section 5.3).

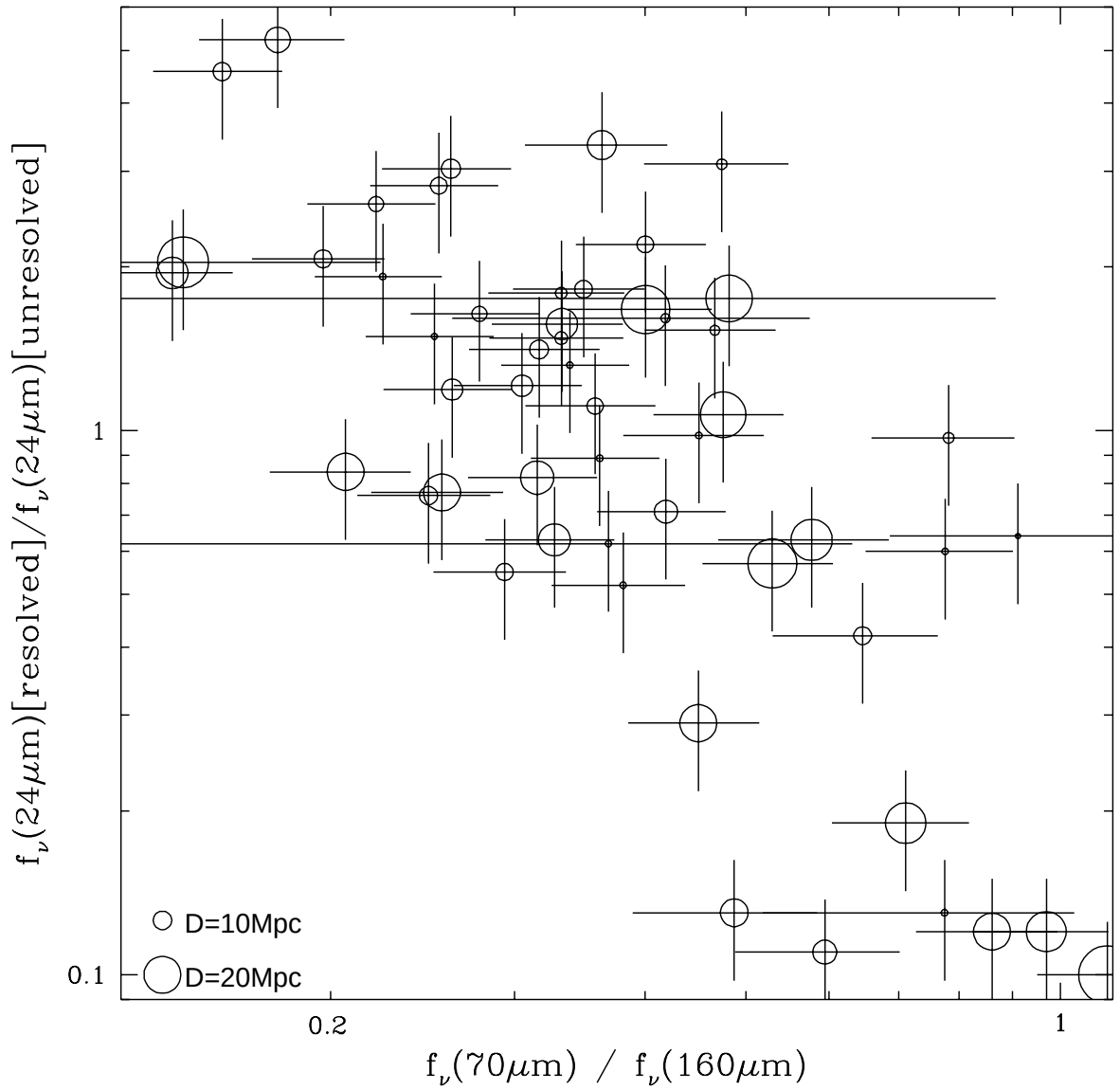

Fig. 16.— The ratio of resolved-to-unresolved 24 μm emission as a function of far-infrared color (see Section 5.3). A 25% uncertainty is used for the error bars in the resolved-to-unresolved ratio. The symbol sizes are scaled according to galaxy distance (see legend).

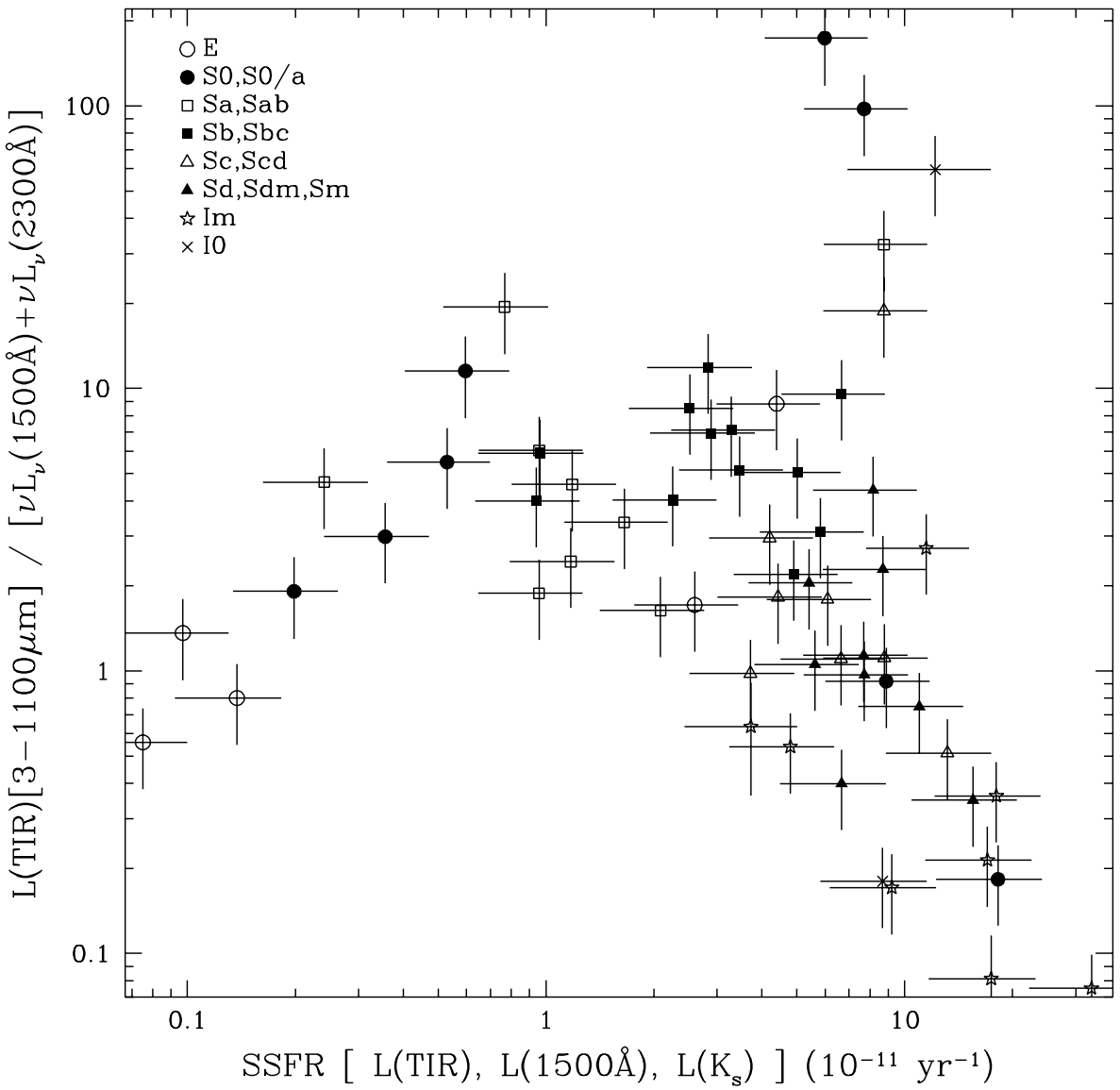

Fig. 17.— The infrared-to-ultraviolet ratio as a function of the specific star formation rate (Equation 5). The error bars derive from the observational uncertainties plus a 30% factor assumed for converting the $K_{\rm s}$ luminosity to a stellar mass (see Section 5.4).

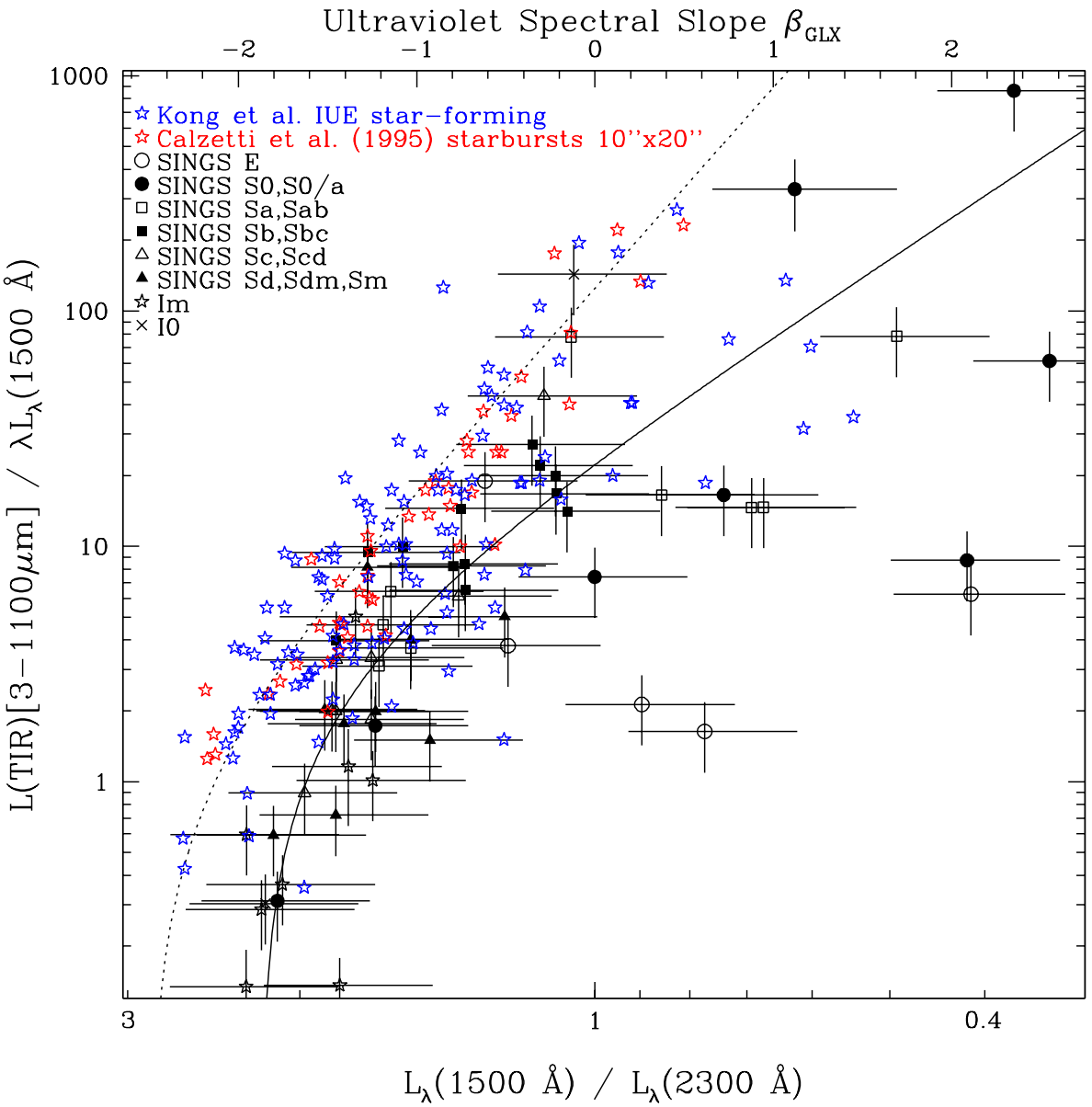

Fig. 18.— The infrared-to-far-ultraviolet ratio as a function of ultraviolet spectral slope. Normal star-forming and starbursting galaxies from Kong et al. (2004) and Calzetti et al. (1995) are plotted in addition to the SINGS data points. The dotted curve is that for starbursting galaxies from Kong et al. (2004) and the solid curve is applicable to normal star-forming galaxies (Cortese et al. 2006).